Efficient Determination of the Uncertainty for the Optimization of SPECT System Design: A Subsampled Fisher Information Matrix

Niccolo Fuin*, Stefano Pedemonte, Simon Arridge, Sebastien Ourselin, and Brian F. Hutton

***Abstract*—System designs in single photon emission tomography (SPECT) can be evaluated based on the fundamental trade-off between bias and variance that can be achieved in the reconstruction of emission tomograms. This trade off can be derived analytically using the Cramer-Rao type bounds, which imply the calculation and the inversion of the Fisher information matrix (FIM). The inverse of the FIM expresses the uncertainty associated to the tomogram, enabling the comparison of system designs. However, computing, storing and inverting the FIM is not practical with 3-D imaging systems. In order to tackle the problem of the computational load in calculating the inverse of the FIM, a method based on the calculation of the local impulse response and the variance, in a single point, from a single row of the FIM, has been previously proposed for system design. However this approximation (circulant approximation) does not capture the global interdependence between the variables in shift-variant systems such as SPECT, and cannot account e.g., for data truncation or missing data. Our new formulation relies on subsampling the FIM. The FIM is calculated over a subset of voxels arranged in a grid that covers the whole volume. Every element of the FIM at the grid points is calculated exactly, accounting for the acquisition geometry and for the object. This new formulation reduces the computational complexity in estimating the uncertainty, but nevertheless accounts for the global interdependence between the variables, enabling the exploration of design spaces hindered by the circulant approximation. The graphics processing unit accelerated implementation of the algorithm reduces further the computation times, making the algorithm a good candidate for real-time optimization of adaptive imaging systems. This paper describes the subsampled FIM formulation and implementation details. The advantages and limitations of the new approximation are explored, in comparison with the circulant approximation, in the context of design optimization of a parallel-hole collimator SPECT system and of an adaptive imaging system (similar to the commercially available D-SPECT).**

***Index Terms*—D-SPECT, emission tomography, Fisher information, reconstruction image quality, system design.**

Manuscript received July 22, 2013; revised October 23, 2013; accepted November 17, 2013. Date of publication November 26, 2013; date of current version February 27, 2014. This work has been supported by the Engineering and Physical Sciences Research Councilunder Grant EP/G026483/1 and supported by the National Institute for Health Research University College London Hospitals Biomedical Research Centre. *Asterisk indicates corresponding author.*

*N. Fuin is with the Institute of Nuclear Medicine, University College London Hospitals, NW1 2BU London, U.K. (e-mail: niccolo.fuin@uclh.nhs.uk).

S. Pedemonte S. Arridge, and S. Ourselin are with the Center for Medical Image Computing, University College London, NW1 9EE London, U.K. (e-mail: s.pedemonte@cs.ucl.ac.uk).

B. Hutton is with the Institute of Nuclear Medicine, University College London Hospitals, NW1 2BU London, U.K..

Color versions of one or more of the figures in this paper are available online at http://ieeexplore.ieee.org.

Digital Object Identifier 10.1109/TMI.2013.2292805

I. Introduction

OPTIMIZATION of the system design in single photon emission tomography (SPECT) is a difficult problem due to the computational complexity and to the challenges in the mathematical formulation. In recent years there has been an increasing interest in optimizing system designs prospectively, by computer simulation, at low computational cost. Such optimization problems include the choice of a particular type of detector and collimator and tuning of their parameters, as well as the choice of the number of cameras and their position. While such class of design optimization problems may be referred to as hard optimization, the development of adaptive SPECT systems has introduced a second class of soft optimization problems, where the parameters of the imaging system may be modified during acquisition, in order to image certain desired properties of the underlying object and to adapt to the imaging conditions.

In the probabilistic framework, a reconstruction algorithm provides an estimate of the radioactivity distribution. Such estimation is uncertain, due to the limited amount of information that the scan may acquire. Characterization of the uncertainty associated with the measurement of activity enables the comparison of system designs.

A SPECT imaging system can be evaluated based on its performance for a specific imaging task, such as in lesion detection [29]–[34]. Task specific system optimization strategies have been defined and explored by Barrett *et al.* [28]. In these studies the image quality assessment is based on the performance of human and numerical observers in classification, such as the detection of a certain class of tumors. However, optimization criteria that are not dependent on specific classification tasks are advisable in order to design systems that perform well in a number of possibly unforeseen tasks.

SPECT systems may also be evaluated based on the fundamental trade-off between bias and variance that can be achieved in the reconstruction of emission tomograms [20], [1], [2], [4]. Such tradeoffs may be derived analytically using the Cramer-Rao type bounds [9], [18], [19] which imply the calculation and the inversion of the Fisher information matrix (FIM). In the following we employ the FIM formalism to characterize the uncertainty in the reconstruction. Unfortunately, computing, storing and inverting the FIM is not feasible for the typical matrix size of 3-D imaging systems.

In order to tackle the problem of the computational load in inverting the FIM, an approximation has been previously proposed. Qi *et al.* [5] argued that if we are only interested in calculating the properties of an estimator in a single voxel i, it is

acceptable to ignore the nonstationarity of the FIM. The computations are done for voxel i, and therefore only the ith row of the FIM needs to be calculated. This local approximation of the FIM, is obtained by replacing all rows of the FIM with the shifted version of its ith row and then by inverting this shift-invariant matrix in order to estimate the variance in each voxel i. Consequently, the FIM simply reduces to a circulant matrix and this approximation is referred to as the *circulant approximation*. Using the circulant approximation, in order to estimate the variance in the whole imaging volume, calculations must be therefore be performed for each voxel independently.

However, since the tomographic imaging system measures the integral along lines that traverse the entire imaging volume, the estimate of the activity in a given voxel and its uncertainty are related to the estimate and to the uncertainty in every other location. Since, however, in a SPECT system with parallel hole (PH) collimators, the counts in the detector bins, are the expressions of the integral of the emitted photons originating from a conical volume (and not simply from a line), the interdependence between the voxels becomes even more complex. The full FIM accounts for such complex interdependence between all the voxels in the imaging volume of shift-variant systems such as SPECT; whereas the aforementioned circulant approximation makes use of a single row of the FIM and does not capture such interaction (see Section V).

In this paper, we introduce a novel algorithm for efficient estimation of the uncertainty in the reconstruction, based on the FIM formalism. Our new formulation relies on subsampling the FIM. The FIM is calculated over a subset of voxels arranged in a grid that covers the whole volume. Every element of the FIM at the grid points is calculated exactly, accounting for the acquisition geometry and for the object, without further approximation. This new formulation, presented in Section II-C, reduces the computational complexity in inverting the FIM but nevertheless accounts for the global interdependence between the variables.

The aim of this paper is to describe the new approximation and to explore its use for the optimization of SPECT systems; emphasizing how it enables us to explore the design of highly shift variant systems (as a result of distance dependent resolution, data truncation or adaptive data sampling). Such systems include the standard rotating camera with parallel hole collimator and an adaptive system for cardiac imaging, similar to the commercially available D-SPECT.

This article is organized as follows. Section II-A describes the measurement model and the reconstruction model. Section II-B presents a deterministic method for the estimation of the uncertainty in the reconstruction based on the FIM formalism. Section II-C introduces the new methodology for approximate and efficient calculation of the FIM. Section II-D describes in detail the efficient implementation of the algorithm for the calculation of the FIM. Section II-E introduces a figure of merit for the estimation of the image quality (based on the fundamental trade-off between bias and variance) and its application to system design. Section II-F summarizes the reference statistical method for the calculation of the uncertainty. The statistical method involves the reconstruction of a large number of noise realizations of the same projection data set and is therefore very time consuming. Section III describes several simulation studies, with the purpose of illustrating our novel methodology. We show how our new algorithm applies to the optimization of a parallel hole collimator for SPECT and how it can be employed to evaluate the reconstructed image quality in the case of truncated projection data and for different acquisition protocols for the D-SPECT system. In order to illustrate the reliability of our approximation, all the results presented in this paper are compared with the reference statistical method and with the circulant approximation method. Moreover, we evaluate the effect of the choice of the subsampling scheme for the optimization of the parameters of the aforementioned imaging systems. The results are presented in Section IV and discussion of the usefulness and limitations of the algorithm are presented in Section V.

II. Methods

A. Measurement Model and Reconstruction Model

The 3-D continuous function expressing the rate of emission of γ-radiation is discretized using a voxel basis, where $\boldsymbol{\lambda} = [\lambda_1, \ldots, \lambda_N]^T$ denotes the vector of emission rates, underlying the projection measurements $\boldsymbol{\nu} = [\nu_1, \ldots, \nu_M]^T$. Let x and y denote the in-plane coordinates, z represents the axial coordinates of the discretized volume, N_x, N_y, N_z denote the number of voxels along each direction and $N = N_x \times N_y \times N_z$ denotes the total number of voxels. The probability to observe measurements $\boldsymbol{\nu}$ when the emission rate is $\boldsymbol{\lambda}$, is expressed by the conditional probability distribution function $p(\boldsymbol{\nu}|\boldsymbol{\lambda})$. In emission tomography, the projection measurements $\boldsymbol{\nu}$, when $\boldsymbol{\lambda}$ is known, can be described as the realization of independent random Poisson processes, whose expected outcomes are given by the following discrete linear model:

$$\bar{\nu}_d(\boldsymbol{\lambda}) = \sum_{i=1}^{N} h_{id}\lambda_i \tag{1}$$

$$\bar{\boldsymbol{\nu}}(\boldsymbol{\lambda}) = \boldsymbol{H}\boldsymbol{\lambda} \tag{2}$$

the matrix $\boldsymbol{H}$ is the $M \times N$ system matrix whose elements $\{h_{id}\}$ represent the probability that photons emitted from voxel i are detected in detector unit d. The system matrix models the propagation and detection of unscattered photons, encompassing the depth-dependent response of the collimator, the position-dependent geometric efficiency, the scanning pattern of the detectors, and attenuation through the propagating medium. In this model, we do not take into account the contribution of scattered photons, though the system matrix $\boldsymbol{H}$ may, in principle, encompass scatter events.

An estimator is a rule for calculating an estimate of the unknown variable (the radio-pharmaceutical density $\boldsymbol{\lambda}$) given the observations (the photon counts $\boldsymbol{\nu}$).

In the case of emission tomography, where the conditional probability distribution associated with photon counting is Poisson distributed with expectation $\boldsymbol{H}\boldsymbol{\lambda}$

$$p(\nu_d|\boldsymbol{\lambda}) = \frac{e^{-[\boldsymbol{H}\lambda]_d}([\boldsymbol{H}\boldsymbol{\lambda}]_d)^{\nu_d}}{\nu_d!} \tag{3}$$

the maximum a posteriori (MAP) estimate consists in selecting the value of the unknown variable that maximizes the following cost function:

$$\hat{\boldsymbol{\lambda}} = \arg\max_{\boldsymbol{\lambda}\geq 0} \Phi(\boldsymbol{\lambda}, \boldsymbol{\nu}) = \arg\max_{\boldsymbol{\lambda}\geq 0} L(\boldsymbol{\lambda}, \boldsymbol{\nu}) - \beta R(\boldsymbol{\lambda}) \quad (4)$$

where the log likelihood function L, is given by

$$\begin{aligned} L(\boldsymbol{\lambda}, \boldsymbol{\nu}) &= \log p(\boldsymbol{\nu}|\boldsymbol{\lambda}) \\ &= \sum_d [\boldsymbol{H}\boldsymbol{\lambda}]_d - \nu_d \log([\boldsymbol{H}\boldsymbol{\lambda}]_d) + \log \nu_d! \end{aligned} \quad (5)$$

In this paper, we restrict the discussion to the quadratic penalty function $R(\boldsymbol{\lambda}) = (1/2)\boldsymbol{\lambda}^T \boldsymbol{R}\boldsymbol{\lambda}$, where $\boldsymbol{R}$ is the Hessian of the space-invariant penalty used for regularization and β is the regularization parameter.

B. Estimation of the Uncertainty in the Reconstruction: The Fisher Information Matrix

In this section, we summarize the deterministic approach for the estimation of the uncertainty in the reconstruction. Closed form analytical expressions of the statistical properties (such as mean and variance) of the MAP estimator defined in the previous section are unavailable. The absence of an explicit analytical expression makes it difficult to study the noise properties of the estimator $\hat{\boldsymbol{\lambda}}$, except through numerical simulations (see Section II-F).

A SPECT system may be evaluated based on the fundamental bias variance trade-off of the estimator and one would like to be able to easily study the estimator characteristics over a range of system parameters. In such cases, numerical simulations can be prohibitively expensive and therefore it is useful to have approximate expressions of the covariance of the MAP estimator.

The distribution of the MAP estimates is approximated by a Normal distribution, parameterized by the covariance matrix $\boldsymbol{\Gamma}$. Under such approximation, Fessler has derived the expression of $\boldsymbol{\Gamma}$ for the log-likelihood function of the Poisson model [11]. Using the first-order Taylor series approximation of (4) around the MAP estimate $\hat{\boldsymbol{\lambda}}$ and then applying the chain rule, we can derive the covariance matrix of the MAP estimator to be

$$\boldsymbol{\Gamma}(\hat{\boldsymbol{\lambda}}) \approx [\boldsymbol{F} + \beta \cdot \boldsymbol{R}]^{-1} \cdot \boldsymbol{F} \cdot [\boldsymbol{F} + \beta \cdot \boldsymbol{R}]^{-1} \quad (6)$$

where $\boldsymbol{F}$ is the FIM of the likelihood. Differentiating the logarithm of the Poisson imaging model (3) [8]

$$\begin{aligned} F_{ij}(\boldsymbol{\lambda}) &= -\mathbb{E}\left[\frac{\delta^2}{\delta\lambda_j \delta\lambda_i} \ln p(\boldsymbol{\nu}|\boldsymbol{\lambda})\right] \\ &= \sum_d^M \frac{h_{id}h_{jd}}{\sigma_d^2} = \sum_d^M \frac{h_{id}h_{jd}}{\bar{\nu}_d} = \sum_d^M \frac{h_{id}h_{jd}}{\sum_b^N h_{bd}\lambda_b} \end{aligned} \quad (7)$$

where the variance of the mth measurement σ_d^2 has been substituted with the noiseless projection data $\bar{\nu}_d$.

C. Efficient Calculation of the Fisher Information Matrix: A Subsampled Version of the FIM

In the previous section, we have described how the FIM can be employed to characterize the uncertainty of the reconstruction. Unfortunately, computing the FIM inverse is intractable since we are dealing with a large matrix of size $N \times N = (N_x \times N_y \times N_z)^2$.

A computationally efficient approximation in calculating the inverse of the FIM has been previously proposed for the design of space-variant penalties that yield to space-invariant impulse response functions [15], [16], [5]. Qi *et al.* [5] argued that if it is reasonable to assume that the FIM varies slowly with position and if one is interested in calculating the effects of a quadratic prior in terms of bias and variance in a voxel i, then it is acceptable to ignore the shift-variance of the FIM. The computations are done for voxel i and therefore only the ith row of the FIM needs to be calculated. This local approximation of the FIM is obtained by replacing all rows of the FIM with the shifted version of its ith row and then by inverting this shift-invariant matrix in order to estimate the variance in each voxel i. This approximation is referred to as the *circulant approximation*, since it simply reduces the FIM to a circulant matrix. This makes the computations in (6) tractable as a circulant matrix can be diagonalized using a discrete Fourier transform (DFT). It is then possible to rewrite the formulas of the covariance for a voxel i in Fourier domain as [15]

$$\boldsymbol{\Gamma}_i(\hat{\boldsymbol{\lambda}}) \approx \mathcal{F}^{-1}\left\{\frac{\mathcal{F}\{\boldsymbol{H}^T D[1/\bar{\nu}_d]\boldsymbol{H}\mathrm{e}_i\}}{|\mathcal{F}\{\boldsymbol{H}^T D[1/\bar{\nu}_d]\boldsymbol{H}\mathrm{e}_i\} + \mathcal{F}\{\beta\boldsymbol{R}\mathrm{e}_i\}|^2}\right\} \quad (8)$$

where $\odot$ denotes element-by-element multiplication and the division is an element-by-element division; e_i is the unit basis vector for the voxel i. The function $\mathcal{F}\{\cdot\}$ takes the DFT of its argument and $D[\cdot]$ produces a diagonal matrix whose diagonal entries are the reciprocal of the noiseless projection data $\bar{\nu}_d$. The complex exponentials, represented by the term $[\mathcal{F}\{\mathrm{e}_i\}]^2$, incorporate the appropriate shifts so that the covariance function is "centered" at location i. From (8) we can see how the approximated estimate of $\boldsymbol{\Gamma}$ for a single voxel position i "can be computed with a projection, a backprojection and a few fast Fourier transforms" [20]. The aforementioned method is well suited for the calculation of the uncertainty for systems whose response can be approximated as shift-invariant; or in the case one wants to estimate the local effects that a penalty function has on bias and variance. However this method does not account for the global interdependence between the estimates in all the voxels and therefore can not incorporate the effects of long-range correlations (e.g., evaluation of the effects of data truncation or missing data).

In this paper, we propose a different approach for calculating the inverse of the FIM. This formulation reduces the computational complexity in inverting the FIM but nevertheless accounts for the global interdependence between the variables. The FIM is calculated over a subset of the voxel indexes $\boldsymbol{G} \subset [1, \ldots, N]$ arranged in a grid that covers the whole volume. We define a subsampled version of the FIM calculated over a subset $\boldsymbol{\lambda}_{\boldsymbol{G}}$ of the full set of parameters $\boldsymbol{\lambda}$

$$F_{ij}^G = \sum_{d=1}^M \frac{h_{id}h_{jd}}{\sum_{b=1}^N h_{bd}\lambda_b} \quad \text{with} \quad i, j \in G. \quad (9)$$

This is equivalent to saying that, in the estimation of the covariance, we are accounting for the interdependence between a

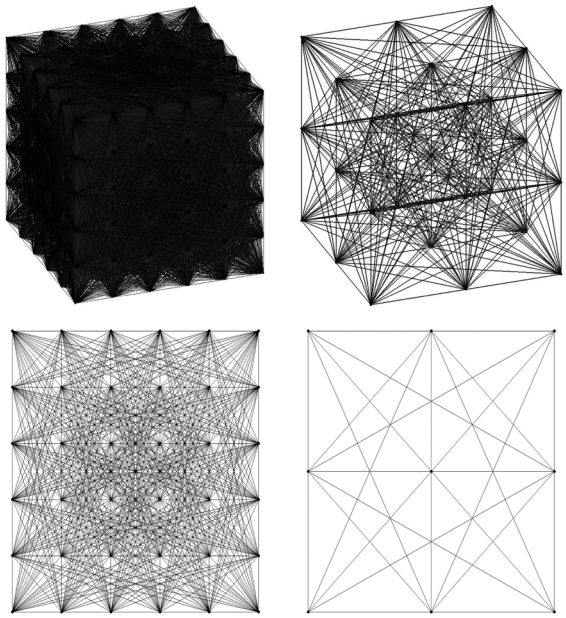

Fig. 1. Example of grids for the estimation of the uncertainty. (a) Grid accounts for the correlation between every point in the imaging volume (full FIM). (b) Grid accounts for the correlation between 1/8 of the voxels in the imaging volume (subsampled FIM). (c) Central plane of the grid displayed in (a). (d) Central plane of the grid displayed in (b).

subset of voxels $i, j \in \boldsymbol{G}$ only, assuming that, for the remaining voxels $i, j \notin \boldsymbol{G}$, the MAP estimate $\hat{\boldsymbol{\lambda}}$ is equal to the true value of $\boldsymbol{\lambda}$.

The approximate analytical calculation of the covariance is simply obtained by substituting the FIM with its subsampled (9) version in the definition of the covariance matrix presented in (6)

$$\boldsymbol{\Gamma}(\hat{\boldsymbol{\lambda}}_G) \approx [\boldsymbol{F}^{\boldsymbol{G}} + \beta \cdot \boldsymbol{R}^{\boldsymbol{G}}]^{-1} \cdot \boldsymbol{F}^{\boldsymbol{G}} \cdot [\boldsymbol{F}^{\boldsymbol{G}} + \beta \cdot \boldsymbol{R}^{\boldsymbol{G}}]^{-1}. \quad (10)$$

The number of elements in the full FIM equals N^2, whereas the number of elements of the subsampled FIM equals N_G^2; therefore reducing the computational burden in inverting the subsampled FIM.

The Hessian of the quadratic penalty $\boldsymbol{R}$ is not dependent on $\boldsymbol{\lambda}$ and therefore can be precalculated. Analogously to F, the subsampled version of the quadratic penalty $\boldsymbol{R}^G$ is obtained by selecting the elements of the matrix $\boldsymbol{R}$ that correspond to the points in the grid.

Two examples of grids are pictured in Fig. 1, for a small imaging volume of $6 \times 6 \times 6$ voxels. In Fig. 1(a), the grid accounts for the interdependence between every point in the imaging volume, in Fig. 1(b), the grid accounts for the interdependence between 1/8 of the voxels in the imaging volume. This model allows the user to design the grid and therefore to define the degree of approximation in the calculation of the FIM. In Section V, visual representations of the FIM and of the covariance matrix are presented for the full FIM, the subsampled FIM, and the circulant approximation. A discussion on how the missing FIM entries between the grid points affect the accuracy of the results is also presented in Section V.

D. GPU Accelerated Implementation

Every element of the FIM at the grid points is calculated exactly, accounting for the acquisition geometry and the object without further approximation. If the grid has N_G nodes, the FIM is of size $N_G \times N_G$ and symmetrical, so filling the matrix requires the computation of $(1)/(2)N_G^2 + (1)/(2)N_G$ elements. Naive computation of the FIM requires one projection for the denominator of (9) and M sums of products (SOPS) for each of the $(1)/(2)N_G^2 + (1)/(2)N_G$ elements of the half FIM. The proposed algorithm is inspired by the rotation-based algorithm proposed by Zeng and Gullberg [6]. The collimator-detector response is captured by a depth dependent point spread function (PSF). Information being additive over the detector bins, the FIM element F_{ij} is the sum of F_{ij}^m contributions from the M camera positions indexed with $m = 1, \ldots, M$. The algorithm is based on interpolation of the activity and of the FIM grid on a regular grid aligned with each camera. By reinterpolating the activity and the FIM grid on a regular grid, the PSF can be applied more efficiently in the frequency domain as all points that are at a given distance lie on the same plane. The PSF is nonzero within a box X (see Fig. 2). The algorithm for the evaluation of the elements of the FIM consists of the following steps.

1) Compute projection of $\boldsymbol{\lambda}$ for each camera position.
2) Compute FIM elements for each camera position.
   a) Re-sample the FIM grid positions on the voxel grid parallel to the camera by tri-linear interpolation.
   b) For each pair of points i, j in the FIM grid.
      i) Compute coordinates of the box Z, on the camera plane, where the two PSFs X_i X_j intersect (if they intersect).
      ii) If X_i and X_j intersect, update the FIM element by integrating (9) over the intersection box Z.

The algorithm is implemented in the CUDA programming language for parallel execution on graphics processing unit (GPU). Tri-linear resampling is performed in hardware by the texture fetch unit of the GPU at the cost of a single memory access. Coalesced memory access is achieved by partitioning the memory transfers in blocks. The convolutions are calculated with the 2-D-FFT and IFFT routines included in the NVidia CUFFT library. A tailor made GPU kernel computes the projection (sum of planes) with high device occupancy and maximizes memory coalescing. A second kernel computes the integral in each intersection box (2-b-ii): each GPU thread computes the integral (for the current camera position), for a pair of points in the grid, so that the integrals for multiple pairs are evaluated concurrently on the multi-processors of the GPU. Each thread decides if the two PSFs intersect, then it loads from the global memory of the GPU device the sections of the PSFs that intersect and the projection data in the area of intersection Z (see Fig. 2). Finally, the thread computes the integral (2-b-ii) in the intersection box. After completion of the partial FIM for a single camera, the process is repeated for another camera, accumulating the elements of the FIM, as, according to (9), information is additive. Computation times are reported in Table I. The GPU-accelerated algorithm for the computation of the FIM has been integrated in the Niftyrec reconstruction software toolbox [21] and has MATLAB and Python interfaces which enable real time scripting interaction and full flexibility in the definition of the grid.

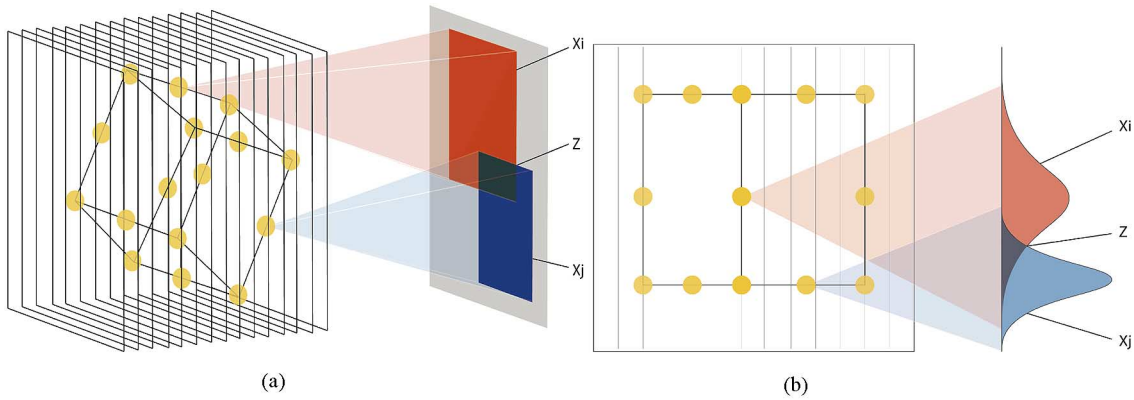

Fig. 2. Rotation-based algorithm for fast computation of the FIM: 3-D schematic representation. Algorithm: 1) for each Gamma camera (grey plane) position, the activity $\boldsymbol{\lambda}$ is resampled on a regular grid parallel to the camera plane and projected; 2) the grid points (yellow spheres) for the FIM are reinterpolated on the same parallel grid; 3) for each pair of points in the FIM grid, the FIM element is updated with the information relative to the current camera, which only depends on the region of the projection Z (black square) where the two PSFs X_i (red square) and X_j (blue square) intersect.

TABLE I
COMPUTATION TIMES FOR THE CALCULATION OF THE FIM AND ITS INVERSE

	g1	g2	g3
Grid Size	27648	6912	3072
NVidia GeForce GTX-285	348s	30s	19s

Reference method	18 hours

E. Image Quality Quantification for System Design

In this paragraph, we introduce a figure of merit for SPECT system design based on the trade-off between the bias and the variance that can be achieved in the reconstruction of emission tomograms.

Under the assumption that the system matrix $\boldsymbol{H}$ in (2) is non-singular and imposing $\beta = 0$ in (4), the maximum likelihood estimator is asymptotically efficient and asymptotically unbiased. One approach to system design, for the unbiased estimator, is to choose the parameters of the imaging system that would produce the least error (minimum variance) in the asymptotic case. This simply involves the inversion of the FIM, to obtain the covariance of the estimator, and is referred to as the Cramer-Rao bound.

However, such approach is problematic because, in practice, the full rank property of the system matrix (nonsingularity) is quite difficult to verify. This problem is addressed by including the regularization penalty of (4) that leads to a strictly convex cost function and makes $\boldsymbol{F} + \beta \cdot \boldsymbol{R}$ in (6) invertible. However bias is unavoidable for penalized estimators, so the unbiased Cramer-Rao bound is not applicable.

The approach that is widely used in emission imaging is to define a local measure of the bias and to consider the trade-off between bias and variance for the optimization of the system. The MAP estimator is nonlinear in the projection data and the properties of the estimator are object dependent. Therefore, we study the bias properties of the estimator locally using the linear local impulse response (LLIR) for the ith voxel [10] (which in the following is referred to as Bias gradient $\boldsymbol{B}$ as in [9])

$$\boldsymbol{B}_i(\hat{\boldsymbol{\lambda}}) = \lim_{\delta \to 0} \frac{\mathbb{E}[\hat{\boldsymbol{\lambda}}(\boldsymbol{\nu}(\boldsymbol{\lambda} + \delta \boldsymbol{e}_i))] - \mathbb{E}[\hat{\boldsymbol{\lambda}}(\boldsymbol{\nu}(\boldsymbol{\lambda})]}{\delta}. \tag{11}$$

This can be approximated using the implicit function theorem, the Taylor expansion, and the chain rule as in [11]

$$\boldsymbol{B}_i(\hat{\boldsymbol{\lambda}}) \approx \boldsymbol{F}^{\boldsymbol{G}} \cdot [\boldsymbol{F}^{\boldsymbol{G}} + \beta \cdot \boldsymbol{R}^{\boldsymbol{G}}]^{-1} \cdot \mathrm{e}_i. \tag{12}$$

In [9], a particular type of MAP estimator including an appropriate space-variant quadratic smoothing prior has been shown to achieve the uniform Cramer Rao bound (UCRB) [9]. However, the space-invariant prior further contributes to space-variance in the bias gradient [15]. Therefore, including and designing an appropriate space-variant penalty function lacks practical justification for the optimization of the design of the imaging system.

To enable comparison between different systems at equal bias gradient, we rely on an adaptation of (10) and (12) where a postsmooth filter $\boldsymbol{P}$ is added to the equations

$$\boldsymbol{\Gamma}(\hat{\boldsymbol{\lambda}}_{\boldsymbol{G}}) \approx \boldsymbol{P}^T \cdot [\boldsymbol{F}^{\boldsymbol{G}} + \beta \cdot \boldsymbol{R}^{\boldsymbol{G}}]^{-1} \cdot \boldsymbol{F}^{\boldsymbol{G}} \cdot [\boldsymbol{F}^{\boldsymbol{G}} + \beta \cdot \boldsymbol{R}^{\boldsymbol{G}}]^{-1} \cdot \boldsymbol{P} \tag{13}$$

$$\boldsymbol{B}_i(\hat{\boldsymbol{\lambda}}) \approx \boldsymbol{P}^T \cdot \boldsymbol{F}^{\boldsymbol{G}} \cdot [\boldsymbol{F}^{\boldsymbol{G}} + \beta \cdot \boldsymbol{R}^{\boldsymbol{G}}]^{-1} \cdot \boldsymbol{P} \cdot \mathrm{e}_i. \tag{14}$$

The penalty function $\boldsymbol{R}$ with a small regularization parameter is included with the only purpose of making the cost function strictly convex. Therefore, the bias property of the estimator is mainly determined by the filter function $\boldsymbol{P}$. In order to compare different systems, we first define a target bias gradient function as an isotropic Gaussian $\boldsymbol{P}_t$ [described by its full-width at half-maximum (FWHM_t)]. Consequently, for every system, an anisotropic postsmooth filter $\boldsymbol{P}$ is designed, so that the bias gradient $\boldsymbol{B}_i$ in (14) matches the target isotropic Gaussian function $\boldsymbol{P}_t$. Designing a specific postsmooth filter for every system under investigation, the noise properties of the estimator can be compared at equal spatially uniform bias gradient. The methodology applied for the design of the postsmooth filter is presented in Appendix A. For more details on how this method compares with UCRB methods, see [18].

We can now reduce (13) and (14) to a scalar measure by taking into account only the variance and the contrast recovery coefficient (CRC) for the voxel i, which we define as $\mathrm{Var}_i = \boldsymbol{\Gamma}_{ii}$ and $\mathrm{CRC}_i = \boldsymbol{B}_{ii}$ (the CRC can be seen as an alternative to the

FWHM as a measure of bias [5]). Thanks to the fixed resolution after postsmoothing, the CRC should be more or less constant; the only parameter to optimize then is the variance. In the rest of this paper, however, we consider the contrast-to-noise ratio (CNR) in voxel i as figure of merit for image quality

$$\mathrm{CNR}_i = \frac{\mathrm{CRC}_i}{\sqrt{\mathrm{Var}_i}}. \tag{15}$$

F. The Statistical Method for the Calculation of the Uncertainty in the Reconstruction

The following reference method was adopted to calculate the uncertainty of the estimation. We can characterize the statistical error in the estimation as the variance of $\hat{\lambda}_d$, computed over a very long series of independent experiments, where the expected measurement values $\bar{\nu}$ are kept fixed, while the noise is sampled from the Poisson distribution. If we consider the hypothetical case where we perform an infinite sequence of experiments, iterating to convergence the algorithm used to maximize the MAP objective function, we obtain estimates that are asymptotically normally distributed. In Section IV we show how, as the number of noise realizations increase, the covariance closely resembles the approximated calculation obtained from (10).

III. Experiments

In the following, we explore the use of the approximate analytical method described in Section II-C for the optimization of the design of SPECT systems. The results obtained with the approximate analytical method are compared with the circulant approximation and with the reference method based on the reconstruction of multiple noise realizations Section II-F. Before this analytical approximation can be applied routinely to evaluate and optimize a SPECT system design, we perform four sets of experiments in order to validate our approximated calculation of covariance (10) and bias gradient (12) in comparison with reference method based on the reconstruction of multiple noise realizations (Section II-F).

For the reference method, a series of independent noise realizations were computed using a pseudo-random Poisson noise generator (of the IRT toolbox [40]), based on the rejection sampling algorithm described in [41, p. 293]. The noisy data sets were reconstructed using an accelerated GPU implementation of the One Step Late algorithm for MAP estimation, implemented as part of the NiftyRec toolbox [21]. 10 000 iterations were performed. A smoothing prior with a small weight $\beta = 10^{-12}$ was included in the cost function. The value of the regularization parameter was chosen after trial and error, as a minimum value that guarantees convergence within 10 000 iterations, as we can see in Figs. 3–5 where the log-likelihood is plotted as a function of the number of iterations. The calculation of the variance is based on 10 240 noise realizations. The number of noise instances is a multiple of 1024 (10 times) as NiftyRec can process concurrently up to 1024 reconstructions in order to make efficient use of the GPU. Ten repetitions were chosen in order to obtain satisfactory images of variance. Though often variance is calculated with much smaller sample size and number of iterations, we found that such large numbers are necessary to obtain a good estimate of the variance.

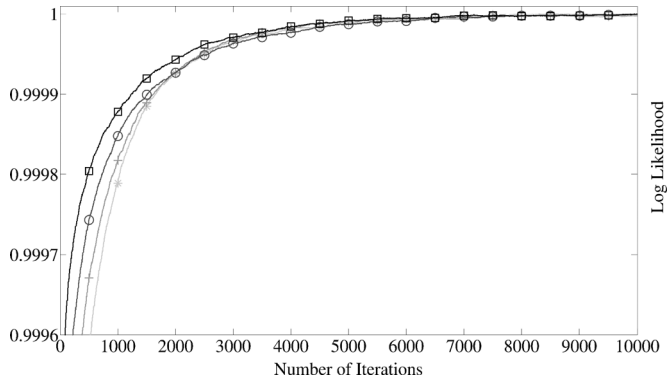

Fig. 3. Log-likelihood curves as a function of number of iterations. Different curves represent the log-likelihood for different collimator apertures: $\mathrm{FWHM} = 5.9$ mm to $\mathrm{FWHM} = 11.08$ mm (from dark gray □ to light gray $*$). All the curves are scaled with respect to their maximum value.

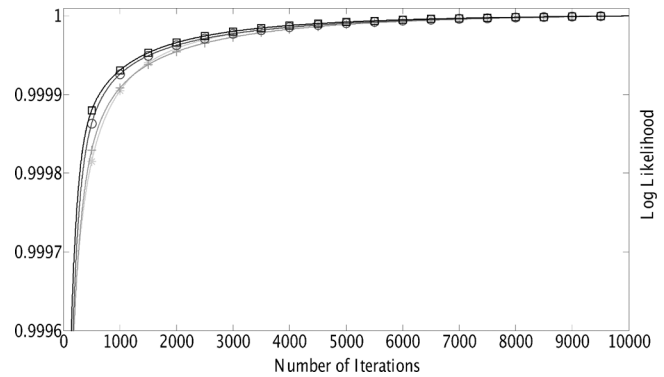

Fig. 4. Log-likelihood curves as a function of number of iterations. Different curves represent the log-likelihood for different levels of truncation. Truncation is caused by a limited detector size. FOV diameter varies from $w = 96$ to $w = 36$ (from dark gray □ to light gray $*$). All the curves are scaled with respect to their maximum value.

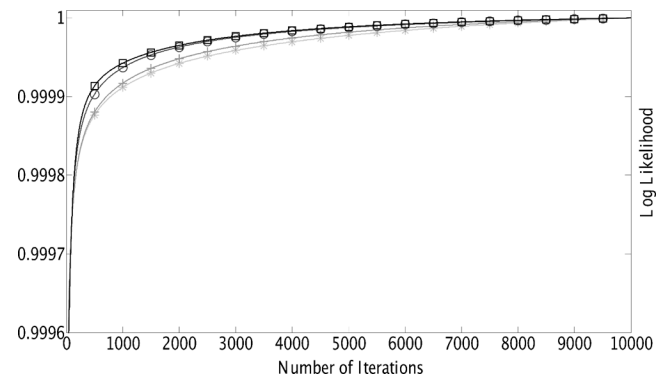

Fig. 5. Log-likelihood curves as a function of number of iterations. Different curves represent the log-likelihood for different scanning patterns of a pD-SPECT system. Scanning pattern is defined by its time ratio S which varies ranging from $S = 0.45$, to $S = 0.9$ (from dark gray □ to light gray $*$). All the curves are scaled with respect to their maximum value.

For the analytical method, the subsampled version of the FIM has been calculated over three different grids of $g_1 = 27\,648$, $g_2 = 6912$ and $g_3 = 3072$ points equally distributed over the slice intersecting the point [or region of interest (ROI)] of interest and the two neighboring slices. We have observed that including more than three slices did not change the results of our experiments in case of full, subsampled, or circulant

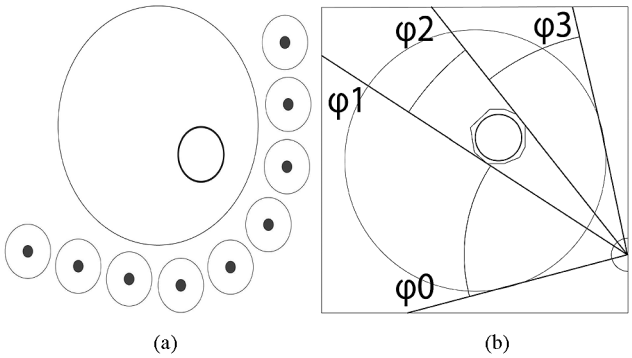

Fig. 6. (a) Position of pD-SPECT detectors. (b) Angular movement of a single pD-SPECT detector. Angular span of the FOV: $\varphi_0 - \varphi_3$. Angular span of the ROI: $\varphi_1 - \varphi_2$.

FIM, since the dependence across slices vanishes quickly with distance along the axis of rotation. Therefore, we have decided to use three slices, in the experiments that follow, for computational convenience. It should be noticed that grid g_1 is fully sampled over the three slices of interest and therefore, in the following, the FIM with grid g_1 will be referred to as the full FIM. The variance images in Fig. 7(b)–(d), Fig. 8(b)–(d), Fig. 9(b)–(d), Fig. 12 (second, third columns), are obtained by reordering the diagonal of the covariance matrix $\mathbf{\Gamma}$ calculated as in (10). For the full FIM (g_1), the diagonal of $\mathbf{\Gamma}$ is simply reshaped to a 3-D matrix, whereas for grids g_2 and g_3 every point of the diagonal of $\mathbf{\Gamma_G}$ is allocated to the respective points of the grid in the imaging volume. A trilinear interpolation is then performed in order to facilitate the visual comparison between the variance images obtained with the different grid models. It should be noticed that a direct interpolation on $\mathbf{\Gamma_G}$ can not be performed. Variance images obtained with the circulant approximation are also presented for comparison. Every pixel of the images in Fig. 7(e), Fig. 8(e), Fig. 9(e), Fig. 12 (fourth column), is calculated according to (8). A more closely spaced grid gives a more precise estimation of the variance but at the cost of increased computational complexity of the estimation. The computation time needed to calculate the FIMs and their inverse are presented in Table I.

We performed four different sets of experiments with different software phantoms and different system models. In Section III-A1, the calculation of the variance obtained from the approximated analytical method (10) is validated for a realistic phantom. In Section III-A2, we employ the approximated calculation of the covariance (10) and bias gradient (12) for the optimization of the collimator aperture. A key challenge in SPECT system design is the achievement of a reasonable trade-off between resolution and detection efficiency. In order to prove the reliability of the proposed approximation, we show that different subsamples of the FIM yield the same optimal collimator aperture. In Section III-A3, in order to emphasize the benefits of the proposed approximation of the FIM with respect to the circular approximation, we investigate how it can be employed to calculate the reconstructed image quality in the case of region-of-interest reconstruction from truncated projection data. In Section III-B1, we employ the proposed novel algorithm for the optimization of the camera trajectory in an adaptive SPECT system. This experiment is also meant to highlight the performance of the new method when used for optimization of systems with a highly shift-variant response, in comparison with other methods for the calculation of the uncertainty, such as the circulant approximation. In the first three experiments (Sections III-A1 –III-A3) we simulate the response of a standard SPECT system, whereas in Section III-B1 we simulate the response of an adaptive system similar to the commercially available D-SPECT system [12]. A description of the two different systems is presented in the following.

A. Circular Camera Trajectory: The SPECT System

The SPECT system is based on a detector system of size 236.16 mm × 236.16 mm. The detector rotates over 360° at a regular angular step of 2° around the center of the imaging volume. The imaging volume dimensions are $96 \times 96 \times 12$ cubic voxels of 2.4 mm. Photon counts are binned on a grid of 96×96 pixels of 2.46 mm and the detector is placed at a distance of 133 mm from the center. We consider a parallel hole collimator consisting of a 2-D array of square holes with septa thickness $s = 0.2$ mm, hole diameter v, and length l. The diameter and the length of the hole are left unknown since they define the collimator aperture. The collimator aperture is characterized by the point spread function (PSF). The PSF for the parallel hole collimator is here described with the analytical depth-dependent model described by Anger [27]. This model expresses the FWHM of the Gaussian at location x, y, z as

$$\mathrm{FWHM}(x,y,z) = \sqrt{\frac{v^2(CD(x,y,z)+l_2)^2}{l_2^2}} \qquad (16)$$

where $CD(x,y,z)$ is the distance between (x,y,z) and the detector plane, $l_2 = l - 2/\mu$ and μ is the total linear attenuation coefficient of the collimator material ($\mu = 22.7$ cm^{-1} for lead at a photon energy of 140 keV). This formula was modified from that presented by Anger [27], by considering that the collimator septa length, l, should be reduced on both ends by approximately $1/\mu$ due to penetration effects [36]. We use the acronym FWHM (without argument (x,y,z)) to denote the collimator aperture that corresponds to the center of the image space. The detector efficiency of a collimator system E is closely related to the collimator aperture and can be defined as the fraction of photons, emitted by a point source in the volume, that are detected in the detector bins if there is no attenuation. For the PH collimator with square holes, E is estimated as

$$E = \frac{v^4}{4\pi l_2^2 (v+s)^2}. \qquad (17)$$

The geometric efficiency is then proportional to the FWHM of the PSF and is assumed to be independent of position. In this study we assume that the detectors have a perfect absorption efficiency and a perfect intrinsic detector resolution.

1) NCAT Phantom: The first experiment is performed simply to validate the analytical method with a realistic phantom. The phantom used for this experiment was a heart phantom (NCAT) [35]. The activity within the phantom was $\lambda = 8$ kBq/cm^3 in the left and right ventricle myocardium, $\lambda = 3.4$ kBq/cm^3 in the left and right ventricle chamber, $\lambda = 0.9$ kBq/cm^3 in the

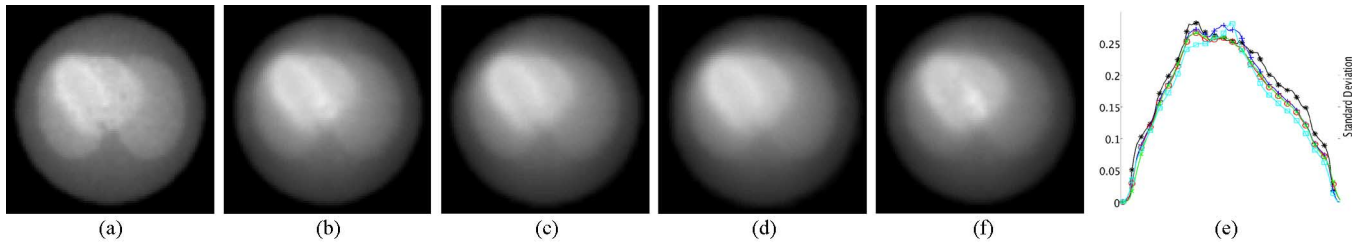

Fig. 7. SPECT: variance images for the NCAT phantom obtained with a standard SPECT system. (a) Reference method (variance image obtained from the reconstruction of 10240 noisy projection data sets). (b) Full Fisher Information-based method with grid g_1. (c) Subsampled Fisher Information based method with grid g_2. (d) Subsampled Fisher Information based method with grid g_3. (e) Variance image obtained with the "Circulant Approximation" method. (f) Variance profiles at the center of the heart: reference method (black line—$*$), grid g_1 (blue line—+), grid g_2 (red line—$\circ$), grid g_3 (green line— $\times$), circulant (cyan line—$\square$).

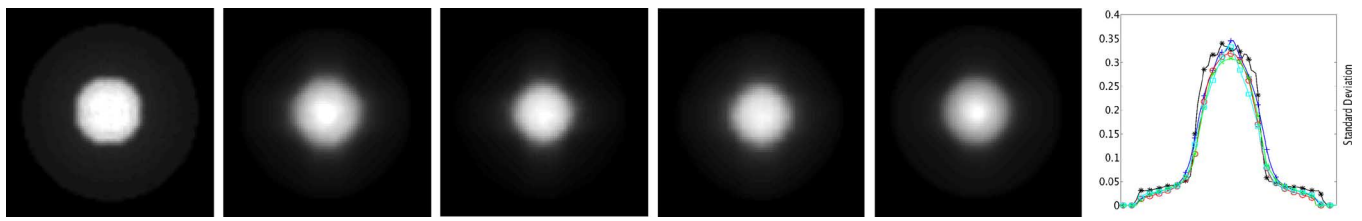

Fig. 8. SPECT: variance images of a uniform sphere obtained with a standard SPECT system. (a) Reference method (variance image obtained from the reconstruction of 10240 noisy projection data sets). (b) Full Fisher Information-based method with grid g_1. (c) Subsampled Fisher Information based method with grid g_2. (d) Subsampled Fisher Information based method with grid g_3. (e) Variance image obtained with the "Circulant Approximation" method. (f) Variance profiles at the center of the heart: reference method (black line—$*$), grid g_1 (blue line—+), grid g_2 (red line—$\circ$), grid g_3 (green line— $\times$), circulant (cyan line—$\square$).

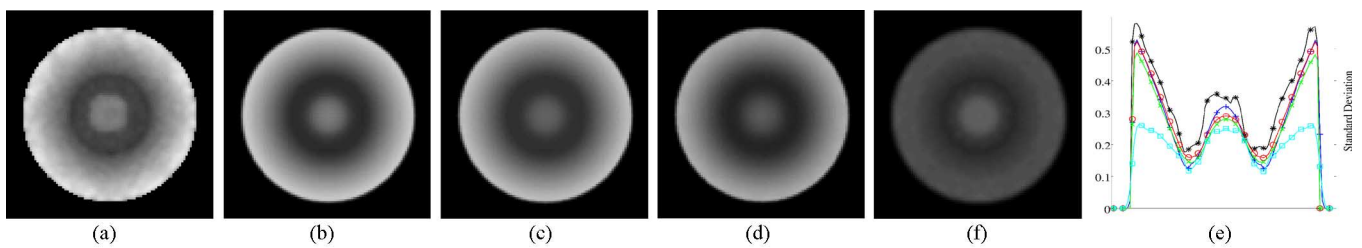

Fig. 9. SPECT interior tomography: variance images for a uniform sphere phantom obtained with truncated projection data with FOV diameter $w = 36$. (a) Reference method (variance image obtained from the reconstruction of 10240 noisy projection data sets). (b) Full Fisher Information-based method with grid g_1. (c) Subsampled Fisher Information based method with grid g_2. (d) Subsampled Fisher Information based method with grid g_3. (e) Variance image obtained with the "Circulant Approximation" method. (f) Variance profiles at the center of the heart: reference method (black line—$*$), grid g_1 (blue line—+), grid g_2 (red line—$\circ$), grid g_3 (green line— $\times$), circulant (cyan line—$\square$).

lungs and $\lambda = 0.6$ kBq/cm^3 in the background. The collimator hole diameter is $v = 1$ mm, collimator hole length $l = 35$ mm, and collimator aperture has FWHM $= 7.89$ mm.

2) Optimal Collimator Aperture: The second experiment is performed to derive the relation between the optimal collimator aperture $\mathrm{FWHM}_{\mathrm{opt}}$ and the target resolution P_t. The phantom used was a uniform sphere positioned at the center of the image space, with diameter $D = 39$ mm. The activity in the sphere was set to $\lambda = 8$ kBq/cm^3 and in the background it was set to $\lambda = 2.4$ kBq/cm^3. During the experiment the collimator aperture varies from FWHM $= 5.9$ mm to FWHM $= 11.08$ mm. The target resolutions are set to $\mathrm{FWHM}_t = 12, 14$, and 16 mm. The CNR for the central point of the sphere is calculated as in (15).

3) Truncated Projection Data: In this experiment we investigate the effect on image variance for region-of-interest reconstruction from truncated projection data. Truncation is caused by a limited detector size. Only a certain number of detector bins w are used to measure data. Note that the field-of-view (FOV) in this truncation situation forms a cylinder whose radius depends on the level of truncation. The phantom was a uniform sphere positioned in the center of the image space, with diameter $D = 24.6$ mm. The uniform background was a cylinder positioned in the center of the image space, with radius 106.3 mm and height 29.5 mm. The activity in the sphere was set to $\lambda = 8$ kBq/cm^3 and to $\lambda = 4.4$ kBq/cm^3 in the background. The size and the position of the sphere has been chosen in order to have the sphere always in the FOV, whereas the activity in the background is gradually more and more outside the FOV with increasing truncation level. During the experiment, the FOV diameter varies from $w = 96$ to $w = 16$ (from 236.2 mm to 39.4 mm). We calculate the variance for a plane intersecting the central point in the sphere and the CNR for a voxel positioned in the center of the sphere.

B. Effect of the Acquisition Trajectory on the Uncertainty of the Measurement: The Adaptive SPECT

The trajectory of the gamma camera has a profound effect on the overall uncertainty of the measurement and on how the uncertainty is distributed throughout the imaging volume. Moving

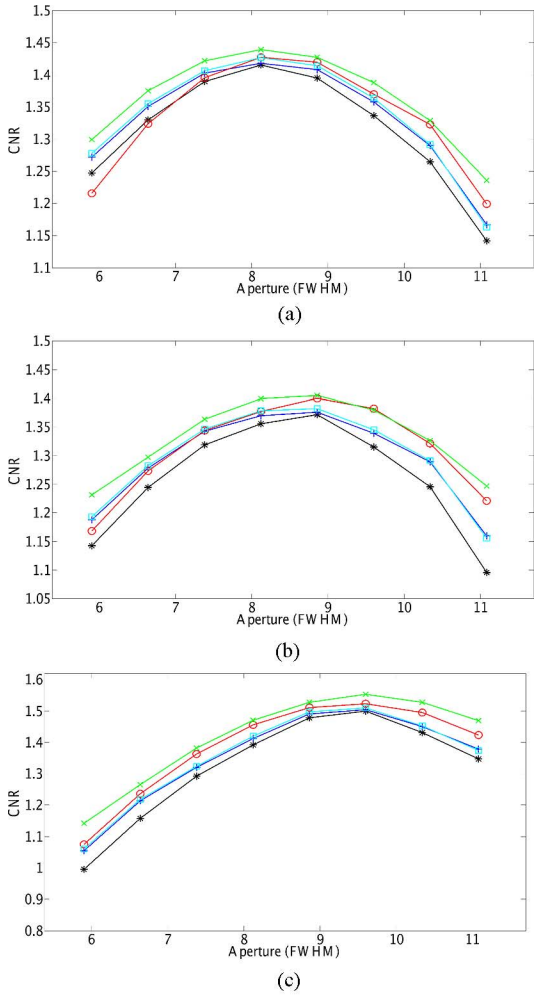

Fig. 10. SPECT: CNRs for different collimator apertures (from $\mathrm{FWHM} = 5.9$ mm to $\mathrm{FWHM} = 11.08$ mm), obtained with the reference method (black line—$*$), with the method based on the Fisher Information with grid g_1 (blue line—+), with grid g_2 (red line—$\circ$), grid g_3 (green line—$\times$) and with the circulant approximation method (cyan line—$\square$). Optimal collimator apertures are calculated for target resolutions $P_{\mathrm{target}} = 12$ mm (a), 14 mm (b), and 16 mm (c).

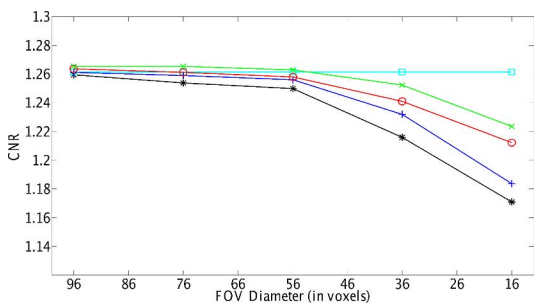

Fig. 11. SPECT interior tomography: CNR for different levels of truncation for a voxel in the center of the sphere. FOV diameter (from left to right) $w = 96, \ldots, 16$. Black line ($*$)—CNR obtained with the reference method. Blue line (+)—CNR obtained with full FIM method with grid g_1. Red line ($\circ$)—CNR obtained with subsampled FIM method with grid g_2. Green line ($\times$)—CNR obtained with subsampled FIM method with grid g_3. Cyan line ($\square$)—CNR obtained from the circulant approximation method.

the camera along a circular trajectory at constant speed around the center of the imaging volume produces, intuitively, optimum retrieval of the information when the object is (roughly) uniform and the PSF ideally not depth-dependent. Changing the trajectory, just like for any other parameter of the acquisition system, the interdependence of the information changes [26]. We consider an adaptive SPECT system similar to the D-SPECT [12], as an example of a system in which the camera trajectory can be modified in response to the characteristics of the underlying activity distribution. In the following we refer to this adaptive SPECT system as the *pseudo* D-SPECT (pD-SPECT).

1) Comparison of Different Acquisition Protocols for An Adaptive SPECT System: The main aim of this set of experiments is to compare different acquisition protocols for the D-SPECT system and to investigate the influence of the presence of activity outside the ROI in the optimization.

The commercial D-SPECT camera system is based on nine collimated detector columns arranged in a curved configuration in order to conform to the shape of the left side of the patient chest [Fig. 6(a)]. Each detector column is then placed at a different distance from the center of the imaging volume (Table II). The software phantom was a uniform sphere positioned at a mean distance from the detectors of 205 mm. The sphere was then positioned in the half of the FOV closest to the detectors, where there is complete tomographic sampling. The uniform background was a cylinder positioned in the center of the image space, with radius 106.3 mm and height 29.5 mm. The activity in the sphere was set to $\lambda = 8$ kBq/cm^3 and the background the activity was set to three different levels $\lambda_{BK1} = 0.9$ kBq/cm^3, $\lambda_{BK2} = 2.2$ kBq/cm^3 and $\lambda_{BK3} = 4.4$ kBq/cm^3. The image volume dimensions are $96 \times 96 \times 12$ cubic voxels of 2.46 mm.

Each of the nine detector blocks is composed of 16×96 individual pixels with a size of 2.46 mm in both dimensions, resulting in a total detector surface of 39.36 mm $\times$ 236.16 mm. The design of the pD-SPECT differs from the commercially available D-SPECT in both the design of its collimators and the specifications of the acquisition protocol. Each detector block is equipped with a PH collimator with hole diameter $v = 1.03$ mm and collimator length $l = 35$ mm. The FWHMs which depend on the distance of every detector from the center of the FOV, are presented in Table II. During acquisition, each of the nine individual detectors rotates independently around its own central axis in order to cover the whole FOV. The adaptive dynamic sequence consists of two options:

a) Open Sweep Acquisition: Each detector block rotates 110° in order to cover the whole FOV, performing 60 regular angular steps. In order to obtain a more complete tomographic sampling, the complete set of detectors is translated by 9° and the open sweep acquisition is performed for a second time.

b) Region of Interest Acquisition: After a preliminary sweep mode scan, the operator defines a ROI contour. The sequence of acquisition is adapted in order to minimize the uncertainty in the ROI. The search of optimum scanning sequences is constrained by the following algorithm: each detector head covers the full angular span of $\varphi_3 - \varphi_0 = 110°$, performing 60 angular steps $\delta\varphi$ [Fig. 6(b)]:

$$\delta\varphi = \begin{cases} \frac{t((\varphi_3-\varphi_2)+(\varphi_1-\varphi_0))}{T(1-S)}, & \text{if } \varphi_0 < \varphi \leq \varphi_1 \\ \frac{(\varphi_2-\varphi_1)}{TS}, & \text{if } \varphi_1 < \varphi \leq \varphi_2 \\ \frac{t((\varphi_3-\varphi_2)+(\varphi_1-\varphi_0))}{T(1-S)}, & \text{if } \varphi_2 < \varphi \leq \varphi_3 \end{cases} \quad (18)$$

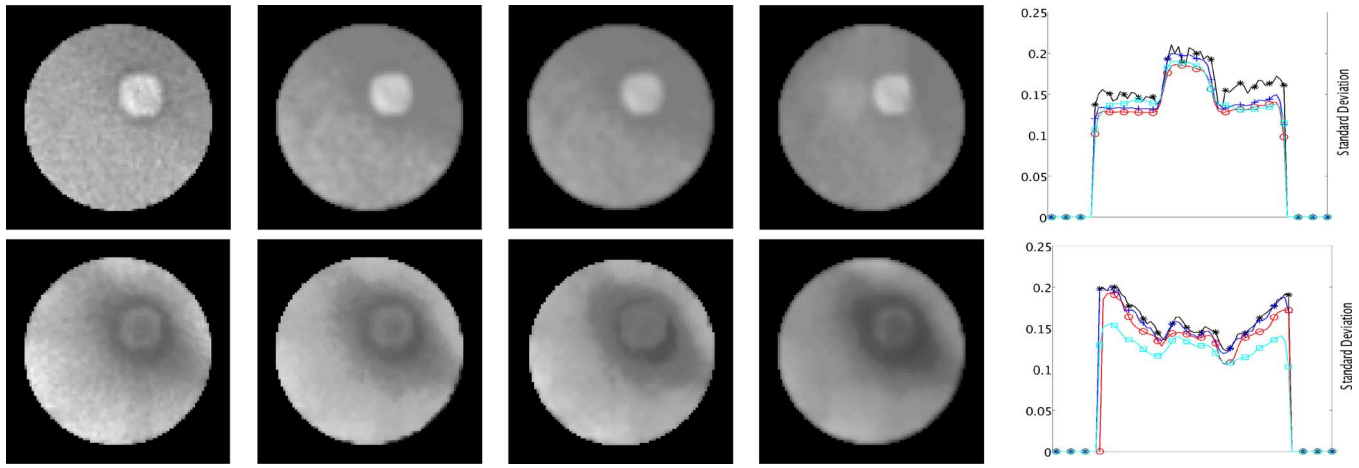

Fig. 12. pD-SPECT: variance images of a uniform sphere ($\lambda = 8$ kBq/cm^3) and uniform background ($\lambda = 2.2$ kBq/cm^3) with scanning pattern time ratio $S = 0.45$ (top row) and $S = 0.9$ (bottom row). First column—reference method (variance image obtained from the reconstruction of 10240 noisy projection data sets). Second column—Fisher Information-based method with grid g_1 (full FIM). Third column—Fisher Information based method with grid g_2. Fourth column—Variance image obtained with the circulant approximation method. Fifth column—Image profiles over a diagonal intersecting the center of the sphere: reference method (black line—$*$), grid g_1 (blue line—+), grid g_2 (red line—$\circ$), circulant approximation method (cyan line—$\square$).

TABLE II
pD-SPECT SYSTEM PARAMETERS

Detector block	1	2	3	4	5	6	7	8	9
Detector distance (mm)	228	203	205	229	248	256	254	249	262
FWHM (mm)	7.93	7.18	7.25	7.97	8.54	8.79	8.70	8.56	8.96

where T is the total scanning time, $t = T/60$ is the constant scanning time for every angular step, φ_1 and φ_2 are the angles subtended by the rays intersecting the center of the detector and tangent to the ROI contour. The complete set of detectors is then translated by 9°; a new set of 60 angular steps is defined and the region centric acquisition is performed a second time. The only parameter defined in order to describe the scanning pattern is the time ratio S that each detector spends acquiring data from the ROI rather than from the surrounding region. We perform, for each of the three different backgrounds in the object, a set of experiments in which the scanning pattern varies ranging from $S = 0.45$, to $S = 0.9$ (where $S = 0.45$ is the time ratio for the open sweep modality). The CNRs are calculated for the central point of the sphere at a constant target resolution $\mathrm{FWHM}_t = 12$ mm.

IV. RESULTS

1) NCAT Phantom: The calculated variance images for the NCAT phantom are shown in Fig. 7. Fig. 7(a) shows the variance image obtained from the reconstruction of 10 240 noisy projection data sets. Fig. 7(b)–(d) shows the corresponding images calculated with the full FIM for grid $g_1 = 27648$ and with the subsampled Fisher Information for grid $g_2 = 6912$ and $g_3 = 3072$, respectively. Fig. 7(e) shows the variance image calculated with the circulant approximation of the FIM. Fig. 7(f) shows the horizontal profiles. From these images we can see how both the method based on the subsampled FIM and the method based on the circulant approximation of the FIM approximately predict the variance of the MAP estimator, presenting minor, but obvious, differences with respect to the variance obtained with the reference method. The variance image obtained from the reconstruction of multiple noise realizations is rather noisy, due to the finite number of repeated experiments (10 240). The variance images predicted with the FIM method, generally speaking, are smooth because neighboring voxels are affected by similar levels of noise. However, a sparser grid gives a more approximated estimation, as we can see in Fig. 7(e). In fact, a fundamental limitation of the subsampled FIM approach is that fine detail is being lost as the grid becomes more sparse. The way the algorithm has been designed permits the degree of approximation in the estimation to be defined by the user. Therefore, a trade-off between computational complexity and reliability of the estimation of the covariance matrix arises. We noticed that, for such a complex phantom, performing the calculation with a grid $g_4 = 1728$ points or less, would lead to incorrect results. The minimum number of grid points necessary to obtain a reliable estimation of the covariance depends on the characteristics of the system under investigation (for a discussion on the selection of the number of grid points, see Section V). Both the method based on the subsampled FIM and the method based on the circulant approximation of the FIM are somewhat less accurate near the edge of the finite support used in image reconstruction, for unknown reasons. This effect (which has been reported also in another study [37]) can lead to a discrepancy exceeding 10% and it is more noticeable, in case of low level of activity, in the off-center voxels of the phantom [25].

2) Optimal Collimator Aperture: Calculated variance images for a uniform sphere phantom at a collimator aperture $\mathrm{FWHM} = 7.89$ mm are displayed in Fig. 8. The variance image obtained from the reconstruction of 10 240 noisy data sets, from the full FIM method, from the subsampled FIM method with different grids and from the circulant approxima-

tion of the FIM method are again in good agreement, as we can see from the horizontal profiles in Fig. 8(f). These results show that the off-center voxels have a lower variance than the central voxels of the phantom. This well-known observation [22] is explained by the fact that, with a SPECT system, some of the planes through off-center voxels have less intersection area with the phantom and are less multiplexed with neighboring voxels than planes through the central voxels.

Fig. 10 shows the optimal collimator aperture for the central point of the sphere obtained with the reference method, with the full FIM (grid g_1), with the subsampled FIM method for grid g_2 and grid g_3 and with the method based on the circulant approximation. The optimal apertures are plotted for the three different target resolutions $P_t = 12$, 14, and 16 mm. From the three plots, we can see how we obtain the same maximum CNR (so in turn, minimum variance) with the reference method, with the full FIM, with the two different subsamples of the FIM and with the circulant approximation method. We can see also how the optimal aperture varies almost linearly in relation with the target resolution imposed in the reconstruction. Similar results were presented in another study [4] which claims that the FWHM of the parallel hole collimator aperture that yields the minimum variance, equals the spatial resolution divided by $\sqrt{2}$.

3) Truncated Projection Data: Fig. 9 shows variance images from truncated projection data with a FOV diameter $w = 36$. The variance image obtained from multiple noisy data sets and the variance images obtained from the full FIM and the subsampled FIM method with different grids are in good agreement. For the voxels outside the FOV, the variance increases considerably in respect to the nontruncated case. Outside the FOV, in fact, we do not have full sampling, since we acquire data from that region only at certain angular positions of the camera. The variance image obtained with the circulant approximation of the FIM method is displayed in Fig. 9(e). From this image, we can notice an increase in variance in the voxels outside the FOV with respect to the nontruncated case. However, the aforementioned effect is less accentuated with respect to the increase in variance estimated with the full FIM method and with the subsampled FIM method in the same region. The horizontal profiles are shown in Fig. 9(f).

In Fig. 11 the CNR for a voxel in the center of the sphere is plotted for different FOV diameters $w = 96, \ldots, 16$. The calculation of the CNR is obtained with the reference method (reconstruction of 1024 noisy data sets), with the novel approach for the approximation of the FIM (with grid of $g_1 = 27\,648$ (full FIM), $g_2 = 6912$, $g_3 = 3072$ points) and, for comparison, with the circulant approximation. Even if (ROI) reconstruction from truncated projections data can lead to nearly unbiased reconstruction in a well-sampled ROI (as demonstrated in [38], [39]), we noticed that a decrease in FOV size leads to an increase in variance (decrease in CNR), not only outside the FOV but also inside it. For this specific experiment we observe a decrease in CNR, for a voxel in the center of the sphere, of 8% compared to the nontruncated case, using the reference method based on multiple noise realizations for the calculation of the variance. An important observation is that we see no effect due to truncation with the circulant approximation of the FIM (as stated in [4]) whereas with the sumbsampled FIM, since we account for the interdependence between the voxels, we see a decreased CNR (increased variance) with increased level of truncation. This is an important feature of the method that we have introduced, because it enables the optimization of systems for interior imaging, which is not possible with existing methods.

4) Comparison of Different Acquisition Protocols for an Adaptive SPECT System: Fig. 12 shows the calculated variance for a slice intersecting the center of the sphere for time ratio $S = 0.45$ and 0.85 (from top to bottom) and background set at $\lambda = 2.2$ kBq/cm^3. The first column shows the results obtained for the reference method for multiple noise realizations. The results obtained with the analytical method based on the inversion of the FIM are shown in the second column for the full FIM characterized by a grid of $g_1 = 27648$ points and in the third column for a subsampled FIM characterized by a grid of $g_2 = 3072$ points. Moreover the results obtained with the circulant approximation of the FIM method are shown in the fourth column. The profiles of the image taken from a diagonal line intersecting the center of the sphere are shown in the fifth column of Fig. 12. From the images obtained with the reference method and with the full and subsampled FIM, we see how with increasing time ratio S, the variance increases in the region outside the ROI whereas the variance in the uniform sphere decreases. This intuitive effect on the uncertainty in the measurements is due to the fact that, with an open sweep acquisition, the entire FOV is scanned uniformly, whereas with increasing time ratio S more time is spent on the ROI at the expense of acquiring less information on the surrounding region. Though the information that is ultimately acquired about the ROI also depends on the information that is acquired in the surrounding region, the net effect of increasing S is to increase the overall information about the activity in the ROI. Once again, for this set of experiments, using the circulant approximation of the FIM method, the aforementioned effect of increasing variance outside the ROI with increasing time ratio S is less accentuated with respect to the increase in variance obtained from the full FIM method and also with respect to the increase in variance obtained from the subsampled FIM method, since the circulant method does not account for effects of long-distance correlations.

The plots in Fig. 13 show the variation of CNR in the central voxel of the sphere for different acquisition protocols whose time ratio varies ranging from $S = 0.45$ to $S = 0.9$. Three experiments were performed for different values of the activity in the background $\lambda_{BK1} = 0.9$ kBq/cm^3 [Fig. 13(a)], $\lambda_{BK2} = 2.2$ kBq/cm^3 [Fig. 13(b)] and $\lambda_{BK2} = 4.4$ kBq/cm^3 [Fig. 13(c)]. From these plots it can be seen that the optimal scanning pattern is sensitive to the level of activity in the background. If the activity in the background is high with respect to the activity in the ROI, an acquisition that more uniformly scans the whole FOV may be preferable. This effect is captured by the subsampled Fisher Information based method with grid g_1 and grid g_2, whereas it is not captured by the circulant approximation of the FIM method. The circulant approximation method only accounts for the increased sensitivity in the ROI with increased time ratio S; whereas it does not account for the effects of long-distance correlations due to a nonuniform scanning pattern.

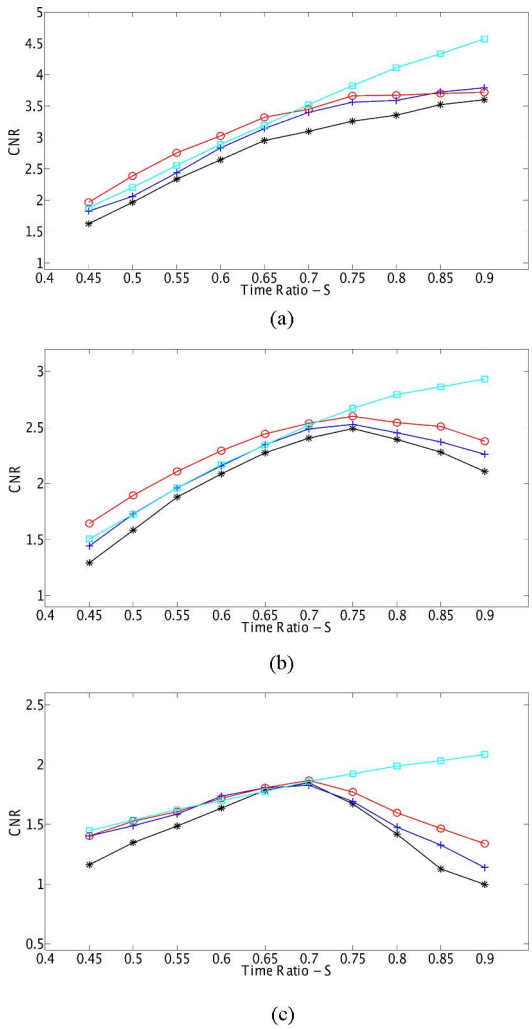

Fig. 13. pD-SPECT: CNRs for different scanning patterns, obtained with the reference method (black line—$*$), with the Subsampled Fisher Information based method with grid g_1 (blue line—+), with the Subsampled Fisher Information based method with grid g_2 (red line—$\circ$) and with the circulant approximation method (cyan line—$\square$). The time ratio ranges from $S = 0.45$ to $S = 0.85$. The optimal time ratios are calculated for different level of background $\lambda_{BK1} = 0.9$ kBq/cm^3 ((A)—top figure), $\lambda_{BK2} = 2.2$ kBq/cm^3 ((B)—central figure) and $\lambda_{BK2} = 4.4$ kBq/cm^3 ((C)—bottom figure). The target resolution $P_{\text{target}} = 12$ remains the same for all the experiments.

It should be noted that the performance of the pD-SPECT system with high level of background changes abruptly (by approximately 50%) when the acquisition parameter changes from $S = 0.7$ to $S = 0.9$ [Fig. 13(c)], while the performance of the SPECT system, with comparable level of background, changes more uniformly across the range of the truncation parameter (Fig. 11). The pD-SPECT system parameterized with $S = 1$ and the truncated single-camera SPECT system are both presenting a data truncation problem. However, the two systems differ substantially in that the SPECT camera rotates by 360° around the center of the imaging volume, acquiring information from all directions, while the nine cameras of the pD-SPECT system are essentially static for $S = 1$, acquiring information from only nine directions. The performance of the D-SPECT system increases abruptly as one moves away from S = 1 due to the increased angular sampling.

V. Discussion

In Section II-A a cost function for the MAP Estimator $\hat{\boldsymbol{\lambda}}$ has been defined. The absence of a closed analytical formulation that expresses $\hat{\boldsymbol{\lambda}}$ explicitly in terms of $\boldsymbol{\nu}$ makes it difficult to study the properties (e.g., mean and covariance) of the MAP estimator $\hat{\boldsymbol{\lambda}}$ defined in Section II-A. For this reason, in order to compare system designs, one has to compute expensive simulations of thousands of reconstructions, as described in Section II-F. The computational complexity of such simulations hinders the online optimization of the parameters of adaptive imaging systems. Alternatively, an approximate estimate of the covariance may be obtained via the FIM, as expressed in (6).

In order to tackle the problem of the computational load in calculating and inverting the FIM, it has been proposed to approximate it with a circulant matrix (see Section II-C). The use of the circulant approximation has been explored for the purpose of measuring the image quality in [9], [10], [5], [15] and for the purpose of system design optimization in [20], [4]. The computational complexity of the reference method, involving the reconstruction to convergence of thousands of noise realizations, has precluded a systematic evaluation of the effect and the limitations of the circulant approximation. For a systematic characterization of the effect of the circulant approximation on the estimates of the covariance matrix, one would have to consider not only a single phantom, but a class of objects. The problem is further complicated by the choice of the regularization parameter β. In this paper, we have described a criterion for the choice of β and a purpose-made GPU accelerated reconstruction software that processes multiple reconstructions in parallel (see Section III), enabling the estimation of the reference variance in a reasonably short time (see Table I). The circulant FIM is generally considered to yield a good approximation of the covariance matrix for nearly shift-invariant systems, however 3-D SPECT systems are inherently shift-variant, even in case of an ideal uniform object in the FOV. Comparison of the variance (the diagonal of the covariance matrix) obtained from the circulant approximation, with the full FIM and with the reference statistical method, has highlighted certain pitfalls of the circulant approximation. The first contribution of this paper consists in having highlighted these effects, described in Section IV. The second and main contribution of this paper is the introduction of a new approximation which relies on a subsampled version of the FIM and that addresses the shortcomings of the circulant approximation (Section II-C).

In the following, the link between the shift-variance of the system and the different approximations of the FIM is illustrated with two examples. Figs. 14 and 16 show the full FIM [Fig. 14(a) and (d) and Fig. 16(a) and (d)] the subsampled FIM with grid g_2 [Fig. 14(b) and (e) and Fig. 16(b) and (e)] and the circulant Fisher matrix [Fig. 14(c) and (f) and Fig. 16(c) and (f)] for the two experiments described respectively in Sections III-A2 and III-A3. The number of elements in the full FIM and in the circulant FIM equals N^2, whereas the number of elements of the subsampled FIM (with grid g_2) equals $(N/2)^2$; therefore highly reducing the computational burden in inverting the subsampled FIM. Since the FIM is a very large matrix and therefore difficult to display, we show the

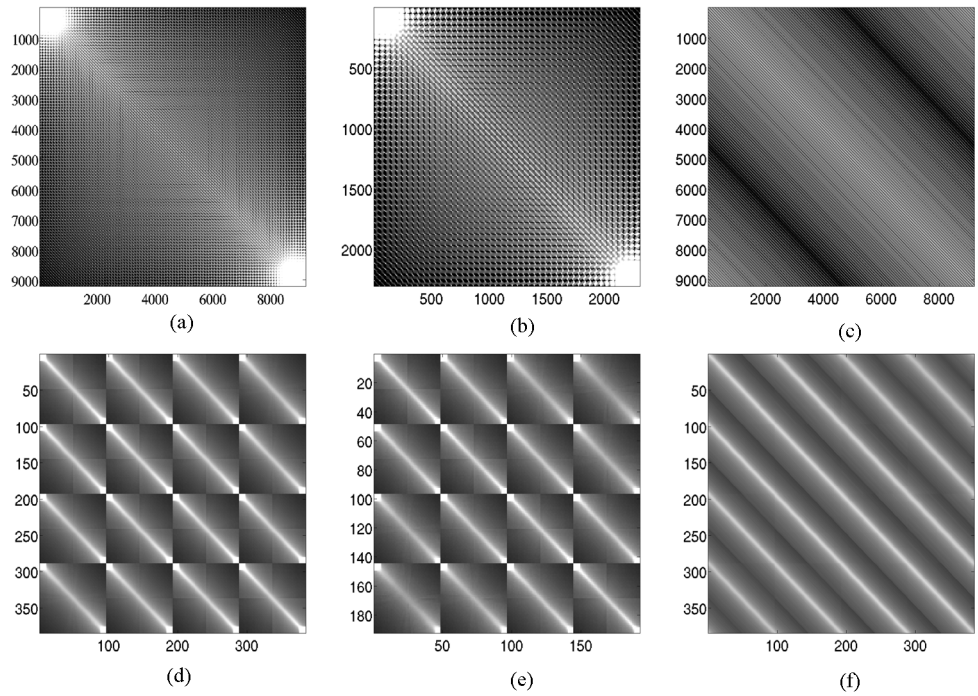

Fig. 14. Fisher Information Matrix for the experiment in Section III-A2. Comparison between full FIM, subsampled FIM and Circulant FIM. (a) Full FIM, grid $g_1 = 9216$ points. (b) Subsampled FIM, grid $g_2 = 2304$ points. (c) Block Circulant with Corculant Blocks FIM for a voxel of interest i in the center of the FOV only. (d) Xoom-in part of A displaying multiple (4 × 4) blocks. (e) Zoom-in part of B displaying multiple (4 × 4) blocks. (f) Zoom-in part of (c) displaying multiple (4 × 4) blocks.

FIMs for the 2-D case. Thus, the full FIM has $g_1 = 9216$ points and the subsampled FIM has $g_2 = 2304$ points. It should be noticed that solving (8), for a voxel of interest i, is equivalent to the inversion of a column of the FIM as if the full FIM were a block circulant matrix with circulant blocks (for the 2-D case), which we refer to as $\tilde{\boldsymbol{F}}$. This is equivalent to creating a new matrix by extracting the ith column from the full FIM, $\tilde{\boldsymbol{F}}^i = \boldsymbol{F}^i$, and then obtaining from this vector the remaining columns of $\tilde{\boldsymbol{F}}$ by an appropriate circulant shift in 2-D so that the peak of $\boldsymbol{F}^i$ becomes centered at the voxel corresponding to each column index. Therefore, we display, in Fig. 14(c) and (f) and Fig. 16(c) and (f), the circulant Fisher matrix for the calculation of the variance of a voxel of interest i in the center of the FOV; whereas we display in Fig. 14(a) and (d) and Fig. 16(a) and (d) the FIM for all the points in the FOV and in Fig. 14(b) and (e) and Fig. 16(b) and (e) the FIM for the points of grid g_2.

As already described in Section II-D, all elements of the subsampled FIM at the grid points are calculated exactly, accounting for the acquisition geometry and for the object. We can see, in fact, how in the subsampled FIM we account for the system response and for the object dependency, whereas with the circulant approximation method we make the assumption that the FIM (and therefore the system response) is shift invariant.

However, what is ultimately of interest is the inverse of the FIM (the covariance matrix). Figs. 15 and 17 show the covariance matrix calculated from the full FIM [Fig. 15(a) and Fig. 17(a)], the covariance matrix calculated from the subsampled FIM with grid g_2 [Fig. 15(d) and Fig. 17(d)] and the covariance matrix calculated using the circulant approximation method [Fig. 15(b) and Fig. 17(b)] for the two experiments described respectively in Section III-A2 and III-A3. Fig. 15(b) and Fig. 17(b) display the covariance matrix obtained by row-by-row inversion of the circulant FIM for the 2-D system, where each column of the matrix is evaluated separately using (8). The resulting covariance matrix is spatially variant (non-circulant) but clearly does not show the same structure as the full FIM inverse in Fig. 15(a) and Fig. 17(a). We can therefore deduce that the circulant FIM can not incorporate the effects of shift-variance, since it does not account for the effects of data truncation or missing data. A direct visual comparison between the inverse of the full FIM and the inverse of the subsampled FIM is arduous, because of the different size of the two matrices. Hence, we show, in Fig. 15(c) and Fig. 17(c), two matrices which are obtained selecting the voxels at the locations of the inverse of the full FIM that correspond to locations of the elements of grid g_2 and then rebinning the selected voxels in a smaller matrix of size $(N/2)^2$. Clearly, the inverse of the subsampled FIM will not be exact at the grid points because of the missing off-diagonal FIM entries between the grid points, however the matrices in Fig. 15(c), Fig. 17(c), and Fig. 15(d), Fig. 17(d) exhibit the same structure. This encompasses the capability of the method to incorporate nonstationary system models and effects of long-range correlations.

The subsampled FIM trades off computational complexity and accuracy of the estimation, enabling the adaptation of the accuracy of the estimation based on the available computational resources. When sufficient resources are available, the GPU-accelerated software described in Section II-D can compute the covariance matrix exactly on a grid g_1. One important advan-

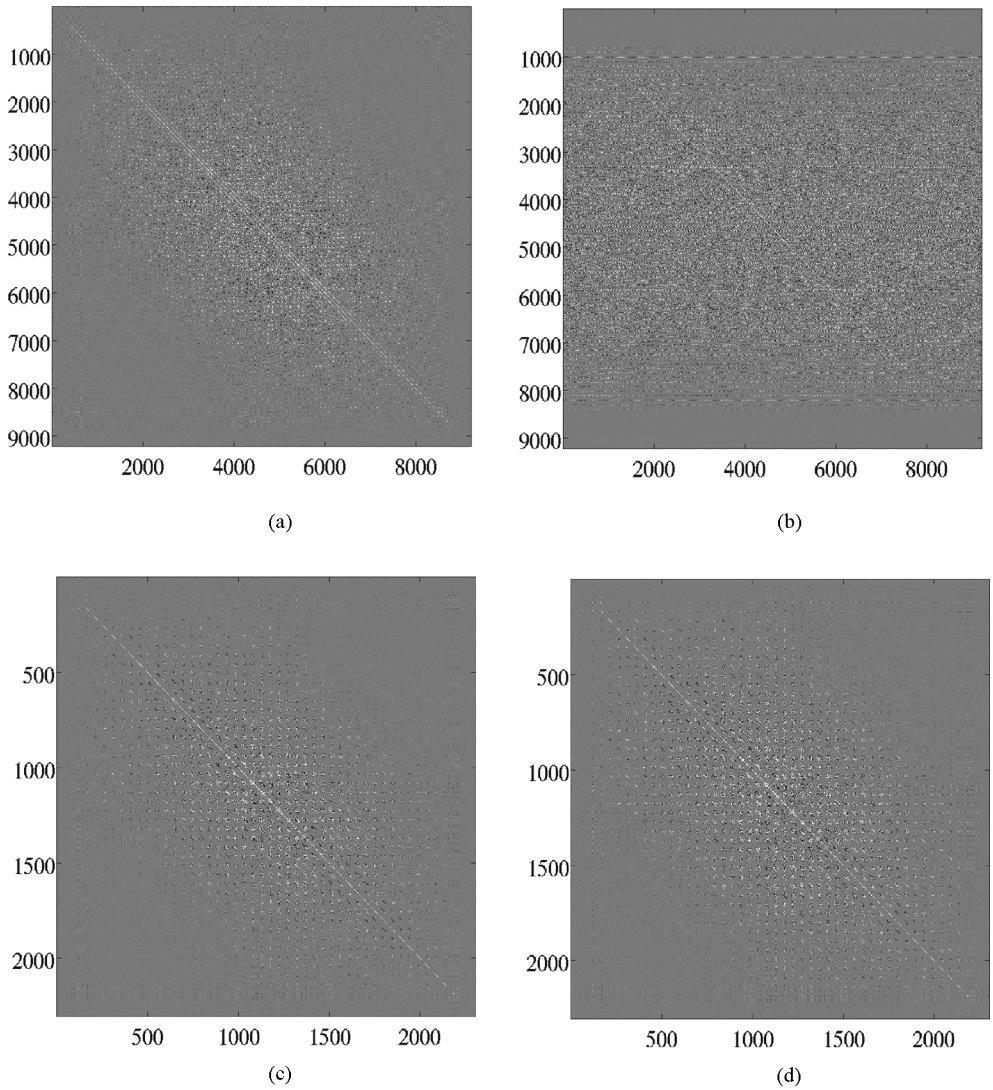

Fig. 15. Inverse of the FIM (covariance matrix) for the experiment in Section III-A2. Comparison between the covariance matrix obtained from the full FIM, the subsampled FIM and obtained by row-by-row inversion of the circulant FIM, where each column of the matrix is evaluated separately using (8). (a) Inverse of the Full FIM, grid $g_1 = 9216$ points. (b) Covariance matrix obtained by row-by-row inversion of the circulant FIM. (c) Covariance matrix obtained by selecting the voxels at the locations of the full FIM that corresponds to locations of the elements of the grid for the subsampled FIM. (d) Inverse of the subsampled FIM, grid $g_2 = 2304$ points.

tage of the scalable subsampled FIM approximation is that the algorithm provides an estimate of the full covariance matrix, though subsampled, accounting for the global interdependence between the variables of the tomogram. This enables the use of global metrics for system design optimization. In other fields of imaging, where the lesser dimensionality of the parameter space enables the storage and inversion of the full FIM, a wide range of global optimality criteria has been explored, such as D-optimality [42] and I-optimality [43]. In the future, a global figure of merit which accounts for the off-diagonal entries of the FIM will be investigated.

Evaluation of the effect of subsampling, however, is complicated by the trade-off that arises. It is not possible to define an absolute criterion for the choice of the subsampling scheme. The contributions to the FIM at a given camera position, for a given pair of grid points, arise only from overlap in the projected PSF from those points (as shown graphically in Fig. 2). The implication is that the grid points must be close enough to ensure there is overlap between the projected PSFs. This condition depends on many factors, including: the image volume size, the voxel size, the size of the PSF, the camera trajectory etc. This condition refers to accuracy of the FIM entry for those two points, but does not apply to accuracy of its inverse, which will suffer from missing points even if the "overlapping PSF" condition is met. Therefore, a general criterion to define a relationship between the subsampling and the reliability of the variance estimation, can not be provided. This criterion depends in fact on the properties of the specific system.

The subsampled FIM formulation and the software tool described in this paper may be employed for the optimization of a range of design parameters of emission imaging systems. However, only three guidelines can be given, so far, for the choice of the subsampling scheme. The first is trivially to adopt the most dense grid for the available computational resources. The second is to restrict the grid volume to a specific region of the FOV, in case we know in advance that activity is present only in

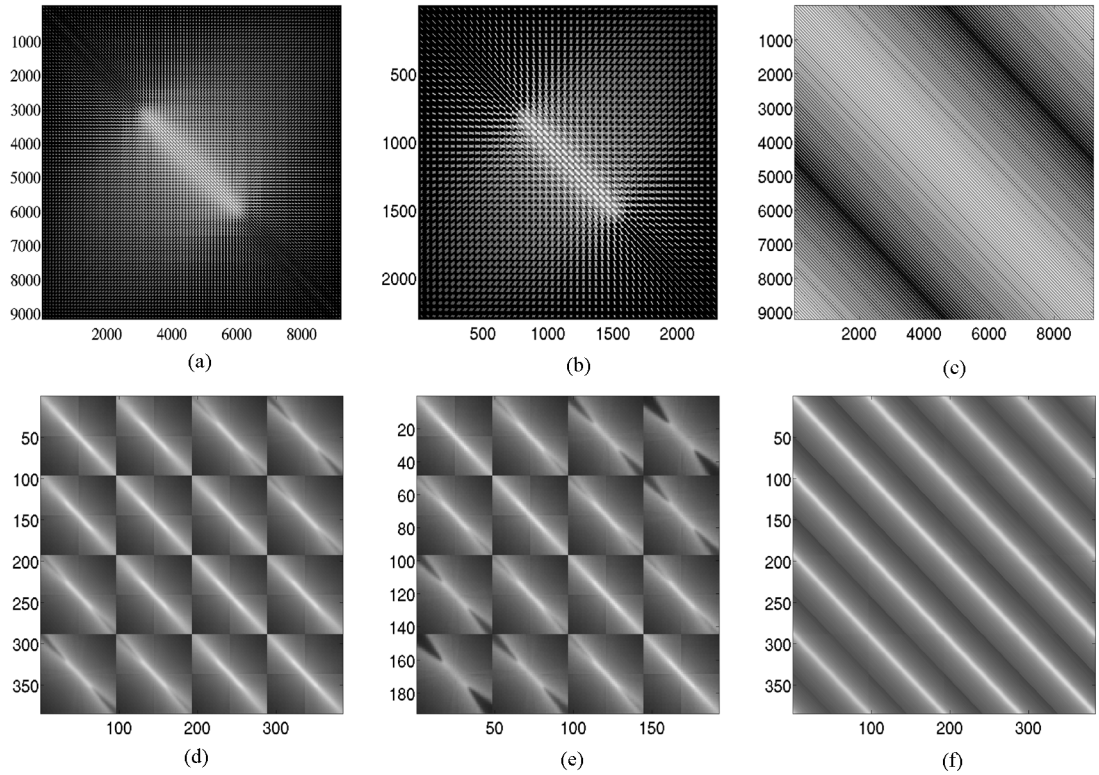

Fig. 16. Fisher Information Matrix for the experiment in Section III-A3. Comparison between full FIM, subsampled FIM and circulant FIM. (a) Full FIM, grid $g_1 = 9216$ points. (b) Subsampled FIM, grid $g_2 = 2304$ points. (c) Block Circulant with Corculant Blocks FIM for a voxel of interest i in the center of the FOV only. (d) Zoom-in part of (a) displaying multiple (4×4) blocks. (e) Zoom-in part of (b) displaying multiple (4×4) blocks. (f) Zoom-in part of (c) displaying multiple (4×4) blocks.

TABLE III
VALIDATION OF THE SUBSAMPLED FIM IN COMPARISON WITH THE REFERENCE STATISTICAL METHOD

Ncat	r2	SEE	a	b
g1	0.9933	2.03 e-04	-0.00413	0.97292
g2	0.9420	2.63 e-04	-0.00433	0.94042
g3	0.9392	3.04 e-04	-0.00454	0.93924
g4	0.9289	0.0046	-0.01069	0.91321
g5	0.9028	0.0061	-0.01803	0.89534

Sphere	r2	SEE	a	b
g1	0.9871	1.62 e-04	-0.00158	0.97934
g2	0.9741	4.47 e-04	-0.00438	0.96172
g3	0.9470	5.72 e-04	-0.00868	0.93471
g4	0.9084	0.0018	-0.01422	0.89297
g5	0.8900	0.0025	-0.01896	0.82733

Inter	r2	SEE	a	b
g1	0.9539	2.33 e-04	-0.0022	0.9529
g2	0.9417	4.90 e-04	-0.0047	0.9106
g3	0.9208	8.25 e-04	-0.0062	0.8687
g4	0.8942	0.0024	-0.0146	0.8174
g5	0.8296	0.0029	-0.0201	0.7955

Dspect	r2	SEE	a	b
g1	0.95928	2.43 e-04	-0.00464	0.94834
g2	0.92837	3.47 e-04	-0.00646	0.89897
g3	0.89902	4.90 e-04	-0.01069	0.81060
g4	0.82983	0.0026	-0.01864	0.79574
g5	0.79345	0.0032	-0.02287	0.76643

that region of interest. The third refers to adaptive imaging systems, where the system adapts during acquisition, in response to the projection data, and therefore where the computational resources are limited by the real-time requirements. For a specific adaptive imaging system and for the specific parameter we want to modify during acquisition, a sufficient condition of optimality needs to be defined. This condition accounts for the trade-off between accuracy of the estimate and computational complexity. Once a sufficient condition of optimality is defined, the subsampling model should be chosen prospectively by comparing the estimates of the optimum scanning parameters for different subsampling models, with the parameters obtained from the reference method.

In Section IV, we prove that the new methodology well predicts how a variation in the system parametrization affects the reconstructed image quality. A validation for the subsampled Fisher Information-based variance calculation method is presented in the following. For every experiment presented in Section III, the variance obtained with the reference statistical method is plotted with respect to the variance predicted with the Fisher information-based method, for grid $g_1 = 27648$ points, grid $g_2 = 6912$ points, grid $g_3 = 3072$ points, grid $g_4 = 1728$ points, and grid $g_5 = 1106$ points. A least square fitting is performed through the data. The regression coefficients, the intercepts of the line, the correlation coefficients and the standard error of the estimate for every experiment are presented in Table III. The sufficient conditions we suggest to obtain a reliable estimate, are that the correlation coefficient between the variance obtained with the reference statistical method and the variance obtained with the subsampled FIM ranges from 0.9 to 1. Also we suggest that the standard error of the estimate should not exceed 0.001. Grid $g_1 = 27648$ points, grid $g_2 = 6912$

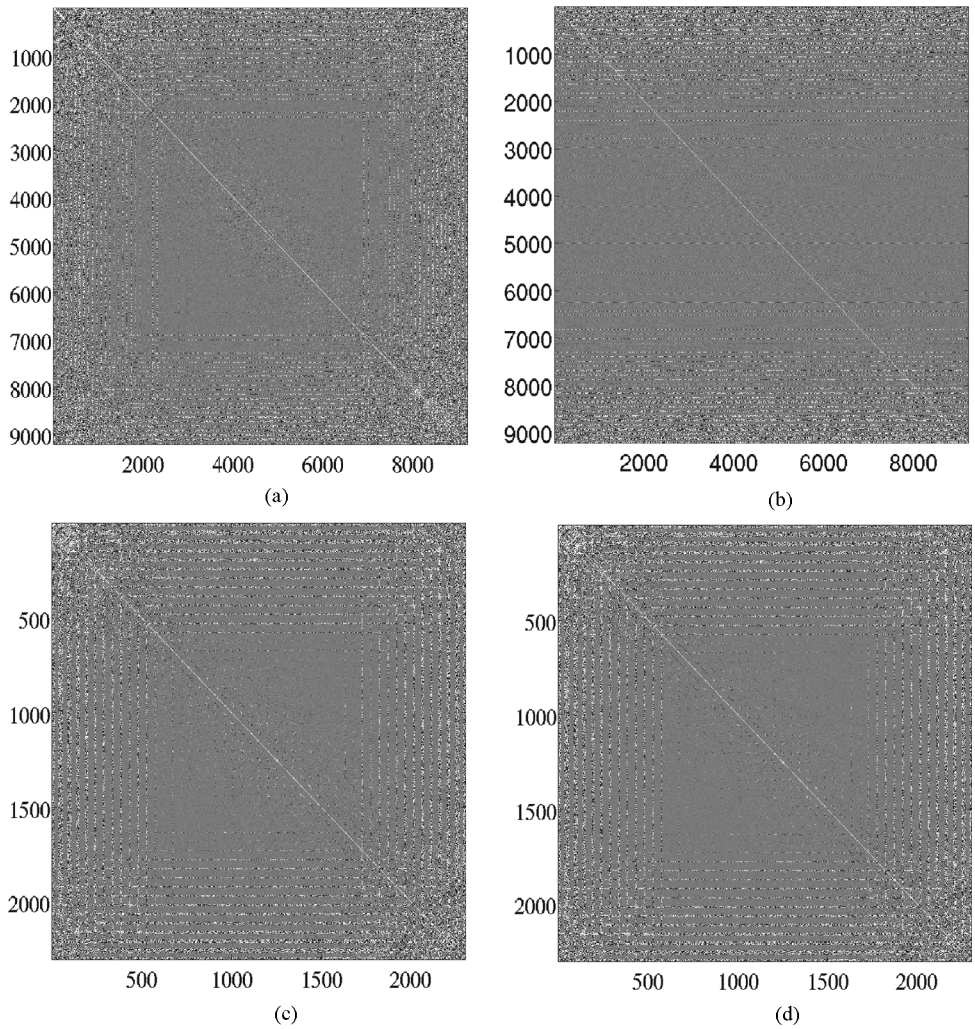

Fig. 17. Inverse of the FIM (covariance matrix) for the experiment in Section III-A2. Comparison between the covariance matrix obtained from the full FIM, the subsampled FIM and obtained by row-by-row inversion of the circulant FIM, where each column of the matrix is evaluated separately using (8). (a) Inverse of the Full FIM, grid $g_1 = 9216$ points. (b) Covariance matrix obtained by row-by-row inversion of the circulant FIM. (c) Covariance matrix obtained selecting the voxels at the locations of the full FIM that corresponds to locations of the elements of the grid for the subsampled FIM. (d) Inverse of the subsampled FIM, grid $g_2 = 2304$ points.

points, and grid $g_3 = 3072$ points satisfy the sufficient condition we suggest for a reliable estimate of the variance. All validation points for the experiment in Section III-A1 for those three grid models are shown in Fig. 18, which plots the standard deviation calculated with the reference method with respect to the standard deviation predicted with the subsampled FIM method. The solid line was fitted to minimize the least squares distance between these points.

The first assumption we make in (7), in order to calculate the FIM, is that the reconstruction is locally linear, meaning that the mean of the noisy reconstruction can be well estimated by the reconstruction of noiseless data. This in turn means that to calculate the FIM we need to know the activity distribution in advance. Fessler and Rogers in [10] argued that even for real noisy measurements we can predict the variance simply by replacing $\bar{\nu}$ with ν in (7). However, this approximation may be problematic and eventually cause convergence problems when the scanning parameters are updated iteratively. The optimization of adaptive systems is still an open problem and needs further investigation.

The calculation of the uncertainty based on the Fisher Information is restricted to problems where $\boldsymbol{\lambda}$ is a continuous parameter in $\mathbb{R}^N$, thus, strictly speaking, its results are not comparable with methods where nonnegativity constraints are imposed on $\hat{\boldsymbol{\lambda}}$. However nonnegativity constraints are active relatively infrequently, so the Fisher Information method can predict the properties of an estimator for most pixels in a phantom. An approach to tackle this problem has been presented by Li *et al.* [25].

In the methodology presented in this paper, a quadratic penalty function with a small weight has been included with the only purpose of enforcing the estimator to have a unique solution and therefore to guarantee the regularized FIM ($[\boldsymbol{F} + \beta \boldsymbol{R}]$) to be invertible. However, since in practice we subsample the matrix, the Hessian of the prior $\boldsymbol{R}$ reduces to a diagonal matrix accounting for the regularization effects only between the voxels in the grid. The use of the circulant approximation of the FIM has been proposed in order to evaluate the local effects of a penalty function on the bias and variance for the shift-invariant system [15].

The experiments presented in this paper account for a uniform attenuation map. If the attenuation map or model for randoms

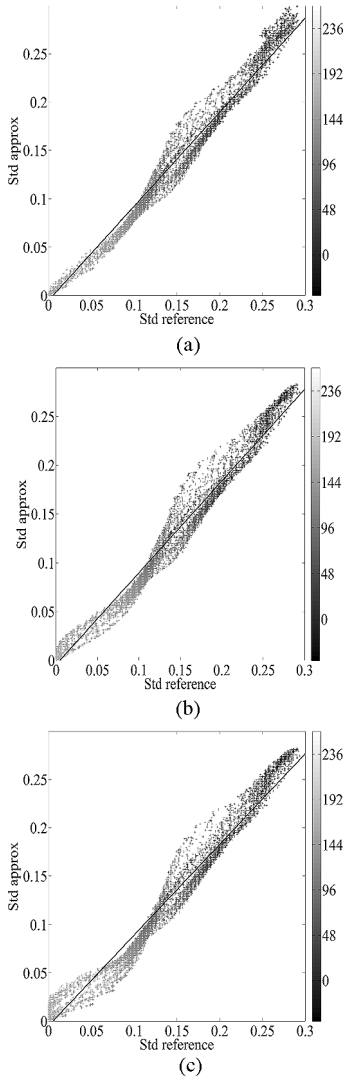

Fig. 18. Validation of the Fisher information-based standard deviation calculation method for different grids. The standard deviation obtained with 10 240 repeated simulations is plotted with respect to the standard deviation predicted with the Fisher information-based method. (a) Grid g_1. (b) Grid g_2. (c) Grid g_3 (from top to bottom). Spatial information is given by the color of the dots. The light gray dots represent voxels which are more distant from the rotation axis (off-center voxels); whereas the dark gray dots represent voxels which are closer to the rotation axis (central voxels). Color bar with the respective distance from the rotation axis (in mm) is displayed for every plot.

and scatter are available, they can be included in the calculation of the FIM to study their effect on image quality, although this is beyond the scope of this paper.

VI. Conclusion

In this paper, we introduce a novel algorithm for the optimization of the system design in emission tomography. The main aim of this new approach is to introduce a less dramatic approximation of the FIM, that still takes into account the global interdependence between the variables. We have applied the method for the estimation of the optimal parameters of a SPECT system, in comparison with the circulant approximation and in comparison with the reference statistical method based on the reconstruction of multiple noise instances. In particular, the novel method has been applied for the choice of a collimator and the tuning of its parameters, and for the choice of the scanning parameters of an adaptive SPECT system.

We have pointed out the shortcomings of the circulant approximation for a range of optimization problems where the system response is markedly shift-variant. In fact, the subsampled FIM method has shown to enable the exploration of design spaces previously precluded by the use of the circulant approximation, such as the evaluation of effects of data truncation in interior tomographic imaging.

The recent development of adaptive SPECT systems has introduced a class of optimization problems where the parameters of the imaging system may be modified in order to image certain desired properties of the underlying object and in order to adapt, during acquisition, in response to the projection data. The D-SPECT is an example of such a system, where the acquisition protocol (in terms of the trajectory of the cameras) can be modified depending on the data acquired during the scan. In order to adapt the response of the system during acquisition, a set of different design parameters have to be compared in real time. Thanks to the novel approximation of the FIM and thanks to an efficient GPU implementation, our novel algorithm for the estimation of the uncertainty, drastically reduces the computational complexity and therefore is a good candidate method for such optimization problems. However, evaluation of the trade-off between computational complexity and accuracy of the estimates for the optimum parameters is an open problem and needs to be evaluated case by case.

The method can be applied to a variety of systems and design parameters in emission computed tomography. The code is available online (URL: http://niftyrec.scienceontheweb.net) and is open source, in order to foster further development and the evaluation of the algorithm for varying imaging conditions and subsampling schemes.

Appendix A
Design of the Postsmooth Filter

A desirable approach to system design optimization is to choose the set of parameters of the imaging system that would lead to the minimum variance in the estimation. However, two different systems parametrizations can be compared by looking at the covariance in the estimation, only if the two systems present the same bias gradient properties.

Standard space-invariant penalties (4) yield to nonuniform bias gradient properties in the reconstructed volume even for space-invariant systems [16]. In order to address this problem a postsmooth filter has been included in (14) and (13). In these equations, a penalty function with a small regularization parameter is added with the only purpose of making the cost function strictly convex and therefore the FIM invertible. Thus, the bias gradient properties of the estimator are determined mainly by the filter function $\boldsymbol{P}$. The method presented in (14) and (13) corresponds to iterating the algorithm used to maximize the MAP objective function (4) to convergence and then convolving the solution with an anisotropic filter $\boldsymbol{P}$ in order to impose a fixed target bias gradient $\boldsymbol{P_t}$. This leads to uniform bias gradient properties in the reconstructed volume.

Relying on this method a postsmooth filter $\boldsymbol{P}$ has to be specifically designed for every system under investigation. A method for the design of this filter is introduced in the following.

Firstly, for every system η, the bias gradient function $\boldsymbol{B}_i^{\kappa}(\hat{\boldsymbol{\lambda}})$ (which is described by its FWHM_η) is calculated as in (11) or (12). An isotropic Gaussian target function $\boldsymbol{P}_t$ is defined so that $\mathrm{FWHM}_t \geq \mathrm{FWHM}_\eta$ (which implies that postsmoothing is always needed to achieve the target bias gradient). The postsmoothing filter $\boldsymbol{P}$ is finally defined taking into account the deviation between the bias gradient $\boldsymbol{B}_i^{\eta}(\hat{\boldsymbol{\lambda}})$ and the target isotropic Gaussian $\boldsymbol{P}_t$

$$\mathcal{P}[k] = \begin{cases} \mathcal{P}_t[k]/\mathcal{B}_i^{\eta}[k], & \text{if } \mathbb{R}(\mathcal{B}_i^{\eta}[k]) \geq 0.005 \\ 0, & \text{if } \mathbb{R}(\mathcal{B}_i^{\eta}[k]) < 0.005 \end{cases} \tag{19}$$

where $\mathcal{P}_t$, $\mathcal{P}$, and $\mathcal{B}_i^{\eta}$ are the Fourier transforms of $\boldsymbol{P}_t$, $\boldsymbol{P}$, and $\boldsymbol{B}_i^{\eta}(\hat{\boldsymbol{\lambda}})$, k is the index of the elements in the Fourier domain and $\mathbb{R}(\cdot)$ denotes the real part of a complex number. Applying the filter $\boldsymbol{P}$ to the bias gradient in (12) ensure that the final bias gradient $\boldsymbol{B}_i(\hat{\boldsymbol{\lambda}})$ in (14) equals $\boldsymbol{P}_t$. The only parameter to optimize then, is the variance $\mathrm{Var}_i = \boldsymbol{\Gamma}_{ii}$ with $\boldsymbol{\Gamma}_{ii}$ calculated as in (13).

REFERENCES

[1] K. Vunckx *et al.*, "Single and multipinhole collimator design evaluation method for small animal SPECT," *IEEE Trans. Med. Imag.*, vol. 27, no. 1, pp. 36–46, Jan. 2008.

[2] K. Vunckx *et al.*, "Effect of overlapping projections on reconstruction image quality in multipinhole SPECT," *IEEE Trans. Med. Imag.*, vol. 27, no. 7, pp. 972–983, Jul., 2008.

[3] K. Vunckx *et al.*, "Fisher information-based evaluation of image quality for time-of-flight PET," *IEEE Trans. Med. Imag.*, vol. 29, no. 2, pp. 311–321, Feb. 2010.

[4] L. Zhou *et al.*, "Comparison between parallel hole and rotating slat collimation: Analytical noise propagation models," *IEEE Trans. Med. Imag.*, vol. 29, no. 12, pp. 2038–2052, Dec. 2010.

[5] J. Qi *et al.*, "Resolution and noise properties of MAP reconstruction for fully 3-D PET," *IEEE Trans. Image Process.*, vol. 19, no. 5, pp. 493–506, 2000.

[6] G. L. Zeng and G. T. Gullberg, "Frequency domain implementation of the three-dimensional geometric point response correction in SPECT imaging," *IEEE Trans. Nucl. Sci.*, vol. 39, no. 5, pp. 1444–1454, Oct. 1992.

[7] S. Kullback and R. A. Leibler, "On information and sufficiency," *Ann. Math. Stat.*, vol. 22, no. 1, 1951.

[8] H. H. Barrett *et al.*, "Objective assessment of image quality: II. Fisher information, Fourier crosstalk, and figures of merit for task performance," *J. Opt. Soc. Am.*, vol. 29, pp. 834–852, 1995.

[9] A. O. Hero *et al.*, "Exploring estimation bias-variance tradeoffs using the uniform CR bound," *IEEE Trans. Sign. Process.*, vol. 44, no. 8, pp. 2026–2040, Aug. 1996.

[10] J. A. Fessler *et al.*, "Spatial resolution properties of penalized-likelihood image reconstruction: Space-invariant tomographs," *IEEE Trans. Image Process.*, vol. 5, no. 9, pp. 1346–1358, Sep. 1996.

[11] J. A. Fessler *et al.*, "Mean and variance of implicitly defined biased estimators (such as penalized maximum likelihood): Applications to tomography," *IEEE Trans. Image Process.*, vol. 5, no. 3, pp. 493–506, Sep. 1996.

[12] K. Erlandsson *et al.*, "Performance evaluation of D-SPECT: A novel SPECT system for nuclear cardiology," *Phys. Med. Bio.*, vol. 54, pp. 2635–2649, 2009.

[13] R. Aharoni and D. Lee, "On the achievability of the Cramer-Rao bound for Poisson distribution," *IEEE Trans. Inf. Theory*, vol. 47, no. 5, pp. 2096–2100, Jul. 2001.

[14] H. Cramer, *Mathematical Methods of Statistics*. Princeton, NJ: Princeton Univ. Press, 1957.

[15] J. W. Stayman and J. A. Fessler, "Regularization for uniform spatial resolution properties in penalized-likelihood image reconstruction," *IEEE Trans. Med. Imag.*, vol. 19, no. 6, pp. 601–616, Jun. 2000.

[16] J. W. Stayman and J. A. Fessler, "Compensation for nonuniform resolution using penalized-likelihood reconstruction in space-variant imaging systems," *IEEE Trans. Med. Imag.*, vol. 23, no. 3, pp. 269–285, Mar. 2004.

[17] J. W. Stayman and J. A. Fessler, "Efficient calculation of resolution and covariance for penalized-likelihood reconstruction in fully 3-D SPECT," *IEEE Trans. Med. Imag.*, vol. 23, no. 12, pp. 1543–1556, Dec. 2004.

[18] L. J. Meng *et al.*, "A modified uniform Cramer-Rao bound for multiple pinhole aperture design," *IEEE Trans. Med. Imag.*, vol. 23, no. 7, pp. 896–902, Jul. 2004.

[19] L. J. Meng *et al.*, "A vector uniform Cramer-Rao bound for SPECT system design," *IEEE Trans. Nucl. Sci.*, vol. 56, no. 1, pp. 81–90, Feb. 2000.

[20] J. Nuyts, "Small animal imaging with multi-pinhole SPECT," *Methods*, vol. 48, no. 2, pp. 83–91, 2009.

[21] S. Pedemonte *et al.*, "GPU accelerated rotation-based emission tomography reconstruction," in *Proc. IEEE Nucl. Sci. Symp. Med. Imag. Conf.*, 2010, pp. 2657–2661.

[22] N. M. Alpert *et al.*, "Estimation of the local statistical noise in emission computed tomography," *IEEE Trans. Med. Imag.*, vol. 1, no. 2, pp. 142–146, Oct. 1982.

[23] H. H. Barrett *et al.*, "Noise properties of the EM algorithm: I. Theory," *Phys. Med. Biol.*, vol. 39, no. 5, pp. 833–846, 1994.

[24] D. W. Wilson *et al.*, "Noise properties of the EM algorithm: II. Monte Carlo simulations," *Phys. Med. Biol.*, vol. 39, no. 5, pp. 847–872, 1994.

[25] Q. Li *et al.*, "Accurate estimation of the fisher information matrix for the PET image reconstruction problem," *IEEE Trans. Med. Imag.*, vol. 23, no. 9, pp. 1057–1062, Sep. 2004.

[26] L. J. Meng and N. Li, "Adaptive angular sampling for SPECT imaging," *IEEE Trans. Nucl. Sci.*, vol. 58, no. 5, pp. 2205–2219, Oct. 2011.

[27] H. Anger, "Scintillation camera with multi-channel collimators," *J. Nucl. Med.*, vol. 5, pp. 515–531, 1964.

[28] H. H. Barrett and K. Myers, *Foundations of Image Science*. New York: Wiley, 2004.

[29] H. H. Barrett *et al.*, "Objective assessment of image quality: III. ROC metrics, ideal observers, and likelihood generating functions," *J. Opt. Soc. Am. Opt. Imag. Sci.*, vol. 15, pp. 1520–1535, 1998.

[30] H. H. Barrett *et al.*, "Objective assessment of image quality: IV. Application to adaptive optics," *J. Opt. Soc. Am. Opt. Imag. Sci.*, vol. 23, pp. 3080–3105, 2006.

[31] P. Khurd and G. Gindi, "Decision strategies that maximize the area under the LROC curve," *IEEE Trans. Med. Imag.*, vol. 24, no. 12, pp. 1626–1636, Dec. 2005.

[32] H. C. Gifford *et al.*, "A comparison of human and model observers in multislice LROC studies," *IEEE Trans. Med. Imag.*, vol. 24, no. 2, pp. 160–169, Feb. 2005.

[33] K. L. Gilland *et al.*, "Comparison of channelized Hotelling and human observers in determining optimum OS-EM reconstruction parameters for myocardial SPECT," *IEEE Trans. Nucl. Sci.*, vol. 53, no. 3, pp. 1200–1204, Jun. 2006.

[34] A. Yendiki and J. A. Fessler, "Analysis of observer performance in known-location tasks for tomographic image reconstruction," *IEEE Trans. Med. Imag.*, vol. 25, pp. 28–41, 2006.

[35] W. P. Segars *et al.*, "Development of a new dynamic NURBS-based cardiac torso (NCAT) phantom," Ph.D. dissertation, , Univ. North Carolina, Chapel Hill, NC, May 2001.

[36] R. J. Jaszczak *et al.*, "Cone beam collimation for single photon emission computed tomography: Analysis, simulation and image reconstruction using filtered backprojection," *Med. Phys.*, vol. 13, no. 4, pp. 484–493, 1986.

[37] Y. Zhang-O-Connor and J. A. Fessler, "Fast predictions of variance images for fan-beam transmission tomography with quadratic regularization," *IEEE Trans. Med. Imag.*, vol. 26, no. 3, pp. 335–346, Mar. 2007.

[38] M. Defrise *et al.*, "Truncated Hilbert transform and image reconstruction from limited tomographic data," *Inv. Prob.*, vol. 22, pp. 1037–1053, 2006.

[39] G. L. Zheng and G. T. Gullberg, "Exact iterative reconstruction for the interior problem," *Phys. Med. Biol.*, vol. 54, no. 19, pp. 5805–5814, 2009.

[40] J. A. Fessler *et al.*, Image Reconstruction Toolbox Jun. 2012 [Online]. Available: http://web.eecs.umich.edu/fessler/irt/irt/

[41] W. T. Vetterling *et al., Numerical Recipes in C*, 2nd ed. Cambridge, U.K.: Cambridge Univ. Press, 2002.

[42] D. A. Delzell *et al.*, "Key properties of D-optimal designs for event-related functional MRI experiments with application to nonlinear models," *Stat. Med.*, vol. 31, no. 29, pp. 3907–3920, 2012.

[43] M. R. Khodja *et al.*, "A heuristic Bayesian design criterion for imaging resolution enhancement," in *IEEE Stat. Sig. Proc. Workshop*, 2012, pp. 9–12.